# Supplementary Materials

# Atomic-Scale Observation of Symmetry Breaking in Altermagnetic MnTe

Guodong Ren[1,*], Jonathan M. DeStefano[2], Xiao-Wei Zhang[1], Arashdeep S. Thind[3], Rajiv Giridharagopal[4], José Ángel Castellanos-Reyes[5], Paul M. Zeiger[1,5], Noah Kamm[3], Sijie Xu[6,7], Zhaoyu Liu[6,7], Yaofeng Xie[2], Filip Krizek[8], Jan Michalička[8,9], Richard Campion[10], Pengcheng Dai[6,7], Peter Wadley[10,11], David S. Ginger[4], Tomas Jungwirth[8,10,11], Robert F. Klie[3], Ján Rusz[5], Di Xiao[1,2], Jiun-Haw Chu[2], Juan Carlos Idrobo[1,12,*]

[1] Department of Materials Science and Engineering, University of Washington, Seattle, WA 98195, USA
[2]Department of Physics, University of Washington, Seattle, WA 98195, USA
[3]Department of Physics, University of Illinois Chicago, Chicago, IL 60607, USA
[4]Department of Chemistry, University of Washington, Seattle, WA 98195, USA
[5]Department of Physics and Astronomy, Uppsala University, Uppsala, Box 516, 75120, Sweden
[6]Department of Physics & Astronomy, Rice University, Houston, TX 77005, USA
[7]Rice Laboratory for Emergent Magnetic Materials and Smalley-Curl Institute, Rice University, Houston, TX 77005, USA
[8]Institute of Physics, Czech Academy of Sciences, Cukrovarnicka 10, 162 00 Prague 6, Czech Republic
[9]Central European Institute of Technology, Brno University of Technology, Purkynova 123, 612 00 Brno, Czech Republic
[10]School of Physics and Astronomy, University of Nottingham, Nottingham NG7 2RD, United Kingdom
[11]Laboratory for Nanoelectronics and Spintronics, Tohoku University, 2-1-1 Katahira, Aoba-ku, Sendai 980-8577, Japan
[12]Physical and Computational Sciences Directorate, Pacific Northwest National Laboratory, Richland, WA 99354, USA

**Contents**

## Section 1. MnTe sample and Néel temperature

The bulk α-MnTe samples in this work were grown by molten Te and Sb flux, respectively. Their representative morphology and dimensions are shown in Figure S1. For each type of samples, two TEM lamellae were prepared along different crystallographic orientations for STEM characterization.

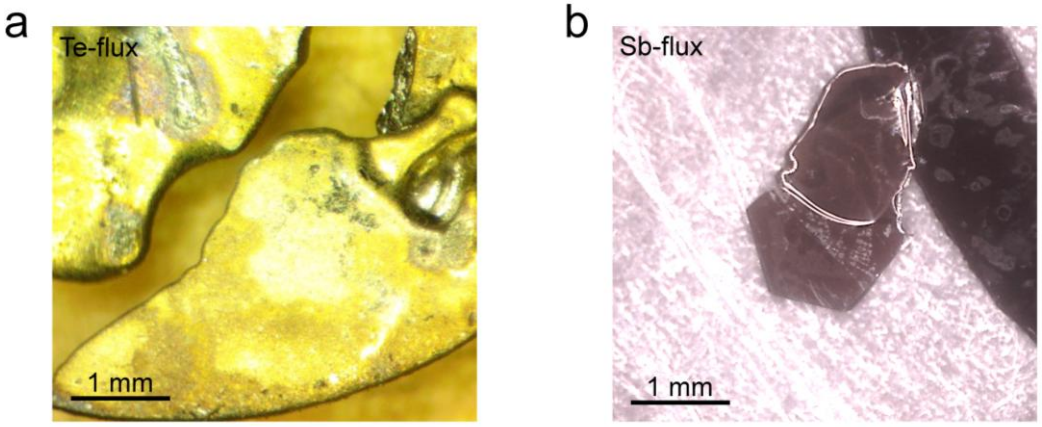


**Figure. S1 Molten flux grown α-MnTe**. **(a-b).** α-MnTe samples grown from molten Te and Sb flux, respectively.

The Néel temperature of the synthesized bulk α-MnTe crystals was determined through temperature-dependent transport and elastocaloric measurements, as shown in Figure S2. Both the resistivity and heat capacity exhibit a kink in slope around 305 K, corresponding to the Néel temperature of α-MnTe crystals.

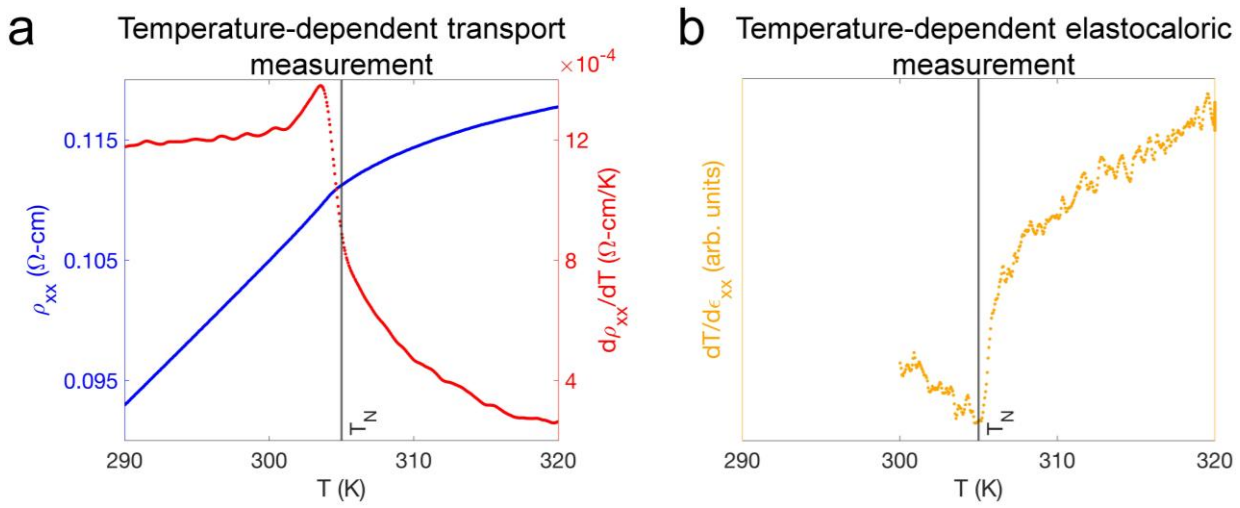


**Figure. S2 Néel temperature measurements of α-MnTe**. Temperature-dependent **(a)** transport and **(b)** elastocaloric measurements of α-MnTe crystal indicating the Néel temperature around 305 K.

**Section 2. Structural distortion measurements in bulk α-MnTe**

To measure the atomic positions with subpixel accuracy, we fitted two-dimensional Gaussians to each atomic column as shown in Figure S3. The Mn and Te columns are identified based on the *Z*-contrast variation. The displacements of Mn were calculated as the offset from the centroid of the $MnTe_6$ octahedra.

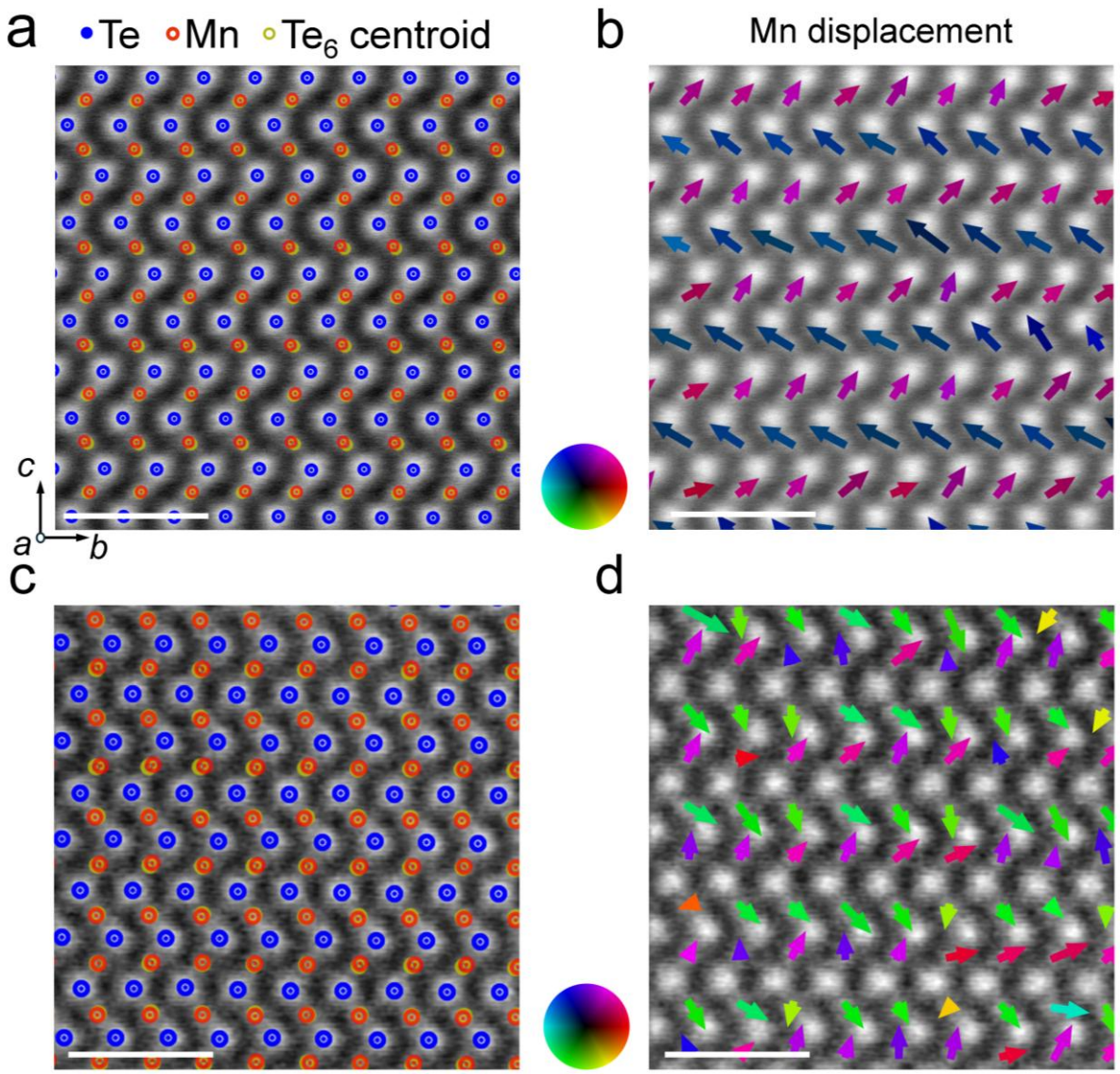


**Figure. S3 Determination of structural distortions arising from Mn displacements**. **(a, c).** Atomic position measurements with two-dimensional Gaussian fitting**. (b, d)** Local structural motifs showing the representative Mn displacement patterns. Scale bars are 1 nm in **(a-d)**.

In Figure S4, multiple structural domains associated with Mn displacement have been directly visualized. Figure S4**a-b** show the coexisting polar domains, with Mn polar displacements along *c*-axis occurring either upward or downward. Oppositely oriented local polar domains and multiple motif families are observed, indicating that the inversion-breaking state is nanoscale and spatially heterogeneous. In addition, Figure S4**c-d** reveal the structural domains consisting of structural motifs of *Amm*2-MnTe and *Cmc*2$_1$-MnTe.

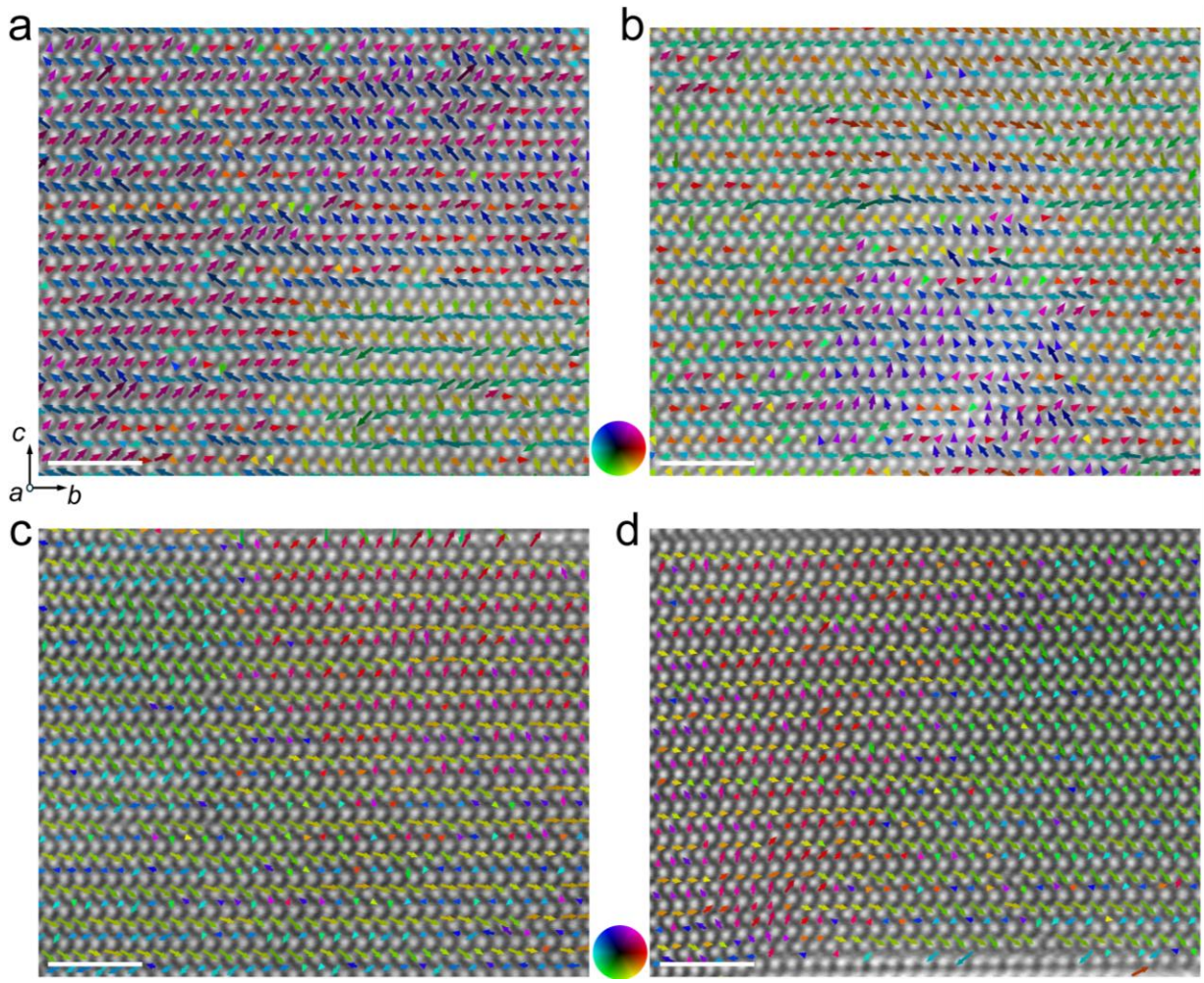


**Figure. S4 Structural domains in α-MnTe**. **(a, b).** The coexisting polar domains with Mn polar displacements along *c*-axis occurring either upward or downward**. (c, d)** Structural domains comprising *Amm*2-MnTe and *Cmc*$2_1$-MnTe structural motifs. Scale bars are 2 nm in **(a-d)**.

In Figure S5, Te sublattice displacements have been evaluated by mapping the Te–Te distances along the vertical ($d_V$) and horizontal ($d_H$) directions, respectively. Figure S5**b** shows uniform horizontal Te-Te spacing which is in contrast to the modulated vertical spacing displayed in Figure S5**c**.

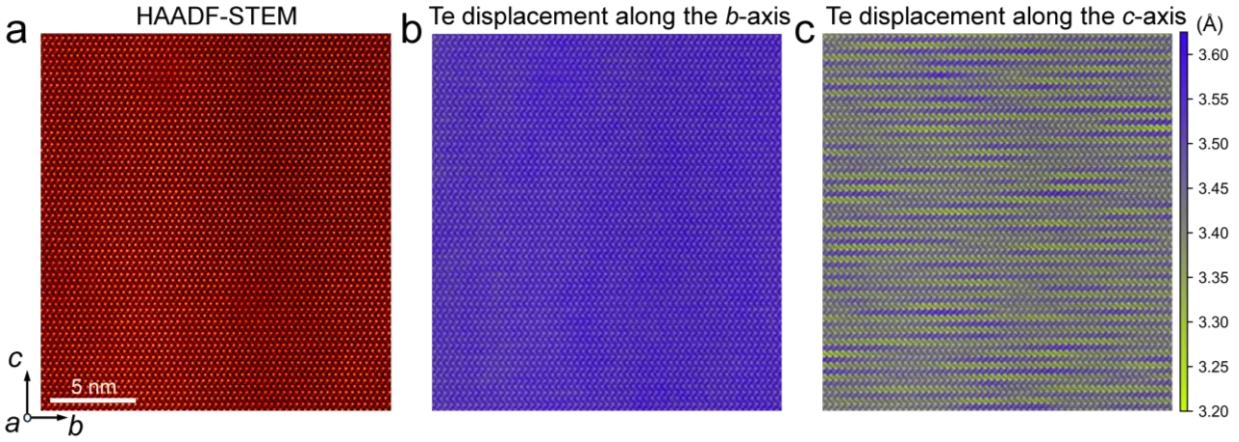


**Figure. S5 Te sublattice displacements**. **(a).** STEM-HAADF image showing the atomic structure of α-MnTe along the *a*-axis**. (b)** Uniform Te-Te distance mapped along the horizontal direction ($d_H$) in the original HAADF image shown in **(a)**. **(c)** Modulated Te-Te distance mapped along the vertical direction ($d_V$).

**Section 3. Structural distortion measurements in α-MnTe thin film**

A ~50 nm thick α-MnTe epilayer was grown by molecular-beam epitaxy (MBE) growth on a single-crystalline InP(111) substrate using elemental Mn and Te sources, similar to the α-MnTe thin film measured in ARPES[1]. TEM lamellae were prepared with C protection layer on the top and finally polished at 2 kV. As shown in Figure S6, the α-MnTe layer exhibits good epitaxy with the InP(111) substrate. Overall, the α-MnTe thin film shows relatively high crystallinity besides a few locally existing dislocations.

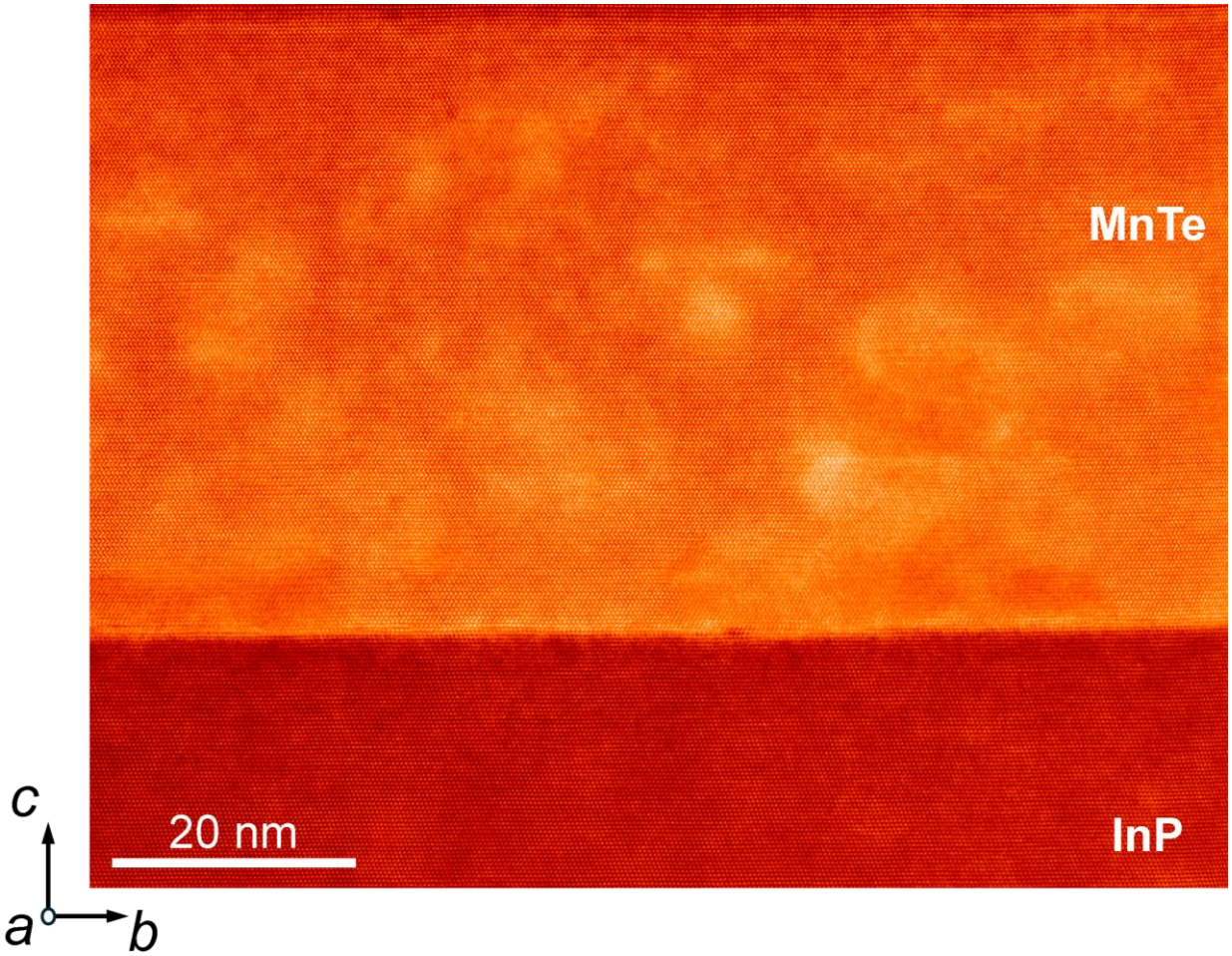


**Figure. S6 α-MnTe thin film epitaxially grown on InP (0001) substrate**. α-MnTe epilayer has a relatively high crystallinity besides a few locally existing dislocations.

In Figure S7 and S8, we performed the same structural analysis on atomic-resolution STEM-HAADF images aquried from α-MnTe thin film. Local structural motif of α-MnTe shown in Figure S7**b** reveals alternating Mn layers undergoing opposite displacements along the horizontal direction, while collectively shifting upward along the vertical direction, corresponding locally to a polar displacement pattern along the *c*-axis. This structural motif resembles the $Cmc2_1$ lattice of bulk sample shown in Figure 2**e** arising from the combined $\Gamma_2^-$ and $\Gamma_5^-$ modes. A statistical analysis of the corresponding Mn-layer displacements is presented in Figure S7**c**: the horizontal components ($u_H$) alternate between positive and negative values, indicating rightward and leftward shifts, whereas the vertical components ($u_V$) are exclusively positive, consistent with a collective upward displacement. The nearest-neighbor Te–Te distances were measured along the vertical ($d_V$) and horizontal ($d_H$) directions, respectively. As shown in Figure S7**d**, Te–Te spacing

exhibits rather uniform spacing along the horizontal direction. The vertical Te–Te spacing exhibits only slight modulation, corresponding to the breathing-type distortions of $\Gamma_3^+$ mode along the *c*-axis. However, this modulation is weaker in the MnTe thin film than in bulk MnTe, as evidenced by the statistical histogram in Figure S7**f**, where both $d_V$ and $d_H$ follow approximately unimodal distributions.

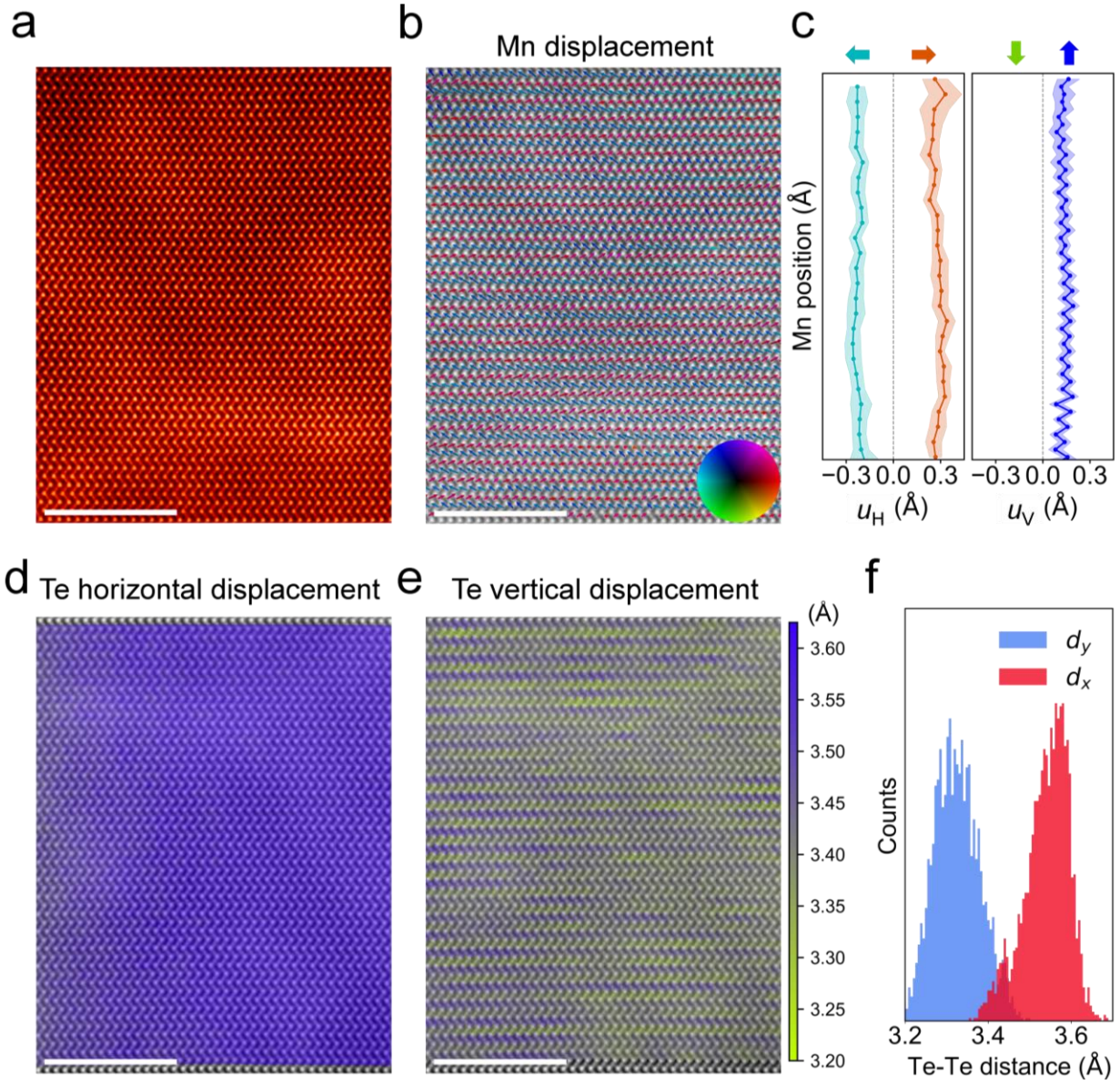


**Figure. S7 Atomic-scale observation of *Cmc*2$_1$ lattice in α-MnTe thin film**. **(a).** A representative STEM-HAADF image showing the atomic structure of α-MnTe thin film along the *a*-axis. **(b).** Displacement vector map of the Mn sublattice. The vectors are calculated from the off-centering of Mn atomic columns relative to the centroid of the surrounding Te sublattice and are overlaid on the original HAADF image shown in **(a)**. **(c).** Statistical analysis of Mn-layer

displacements, corresponding to the local structural motifs shown in **(a)**. Displacements of each Mn layer are resolved along the horizontal ($u_H$) and vertical ($u_V$) directions, respectively. Shaded regions in the plots indicate the corresponding standard deviations. **(d, e).** Nearest Te-Te distance mapping showing relatively uniform Te-Te spacing along the horizontal direction ($d_H$) in **(a)**, but modulated Te-Te spacing along the vertical direction ($d_V$) in **(e)**. **(f).** Histogram plot showing the distribution of Te–Te distances along the vertical ($d_V$) and horizontal ($d_H$) directions in the original HAADF image shown in **(a)**. Scale bars are 5 nm in **(a, b, d, e)**.

In Figure S8, we found the *Amm*2 lattice dominant region. Local structural motif of α-MnTe shown in Figure S8**b** features alternating Mn layers undergoing opposite displacements along the vertical direction while collectively shifting rightward horizontally, corresponding locally to an in-plane polar displacement pattern. The corresponding statistical analysis in Figure S8**c** quantifies the Mn displacements associated with this structural motif. This structural motif resembles the *Amm*2 lattice of bulk sample shown in Figure 2**g** arising from the combined $\Gamma_4^-$ and $\Gamma_6^-$ modes. The nearest-neighbor Te–Te distances were measured along the vertical ($d_V$) and horizontal ($d_H$) directions, respectively. As shown in Figure S8**d**, Te–Te spacing exhibits rather uniform spacing along the horizontal direction. The vertical Te–Te spacing exhibits a slight modulation, corresponding to the breathing-type distortions of $\Gamma_3^+$ mode along the *c*-axis.

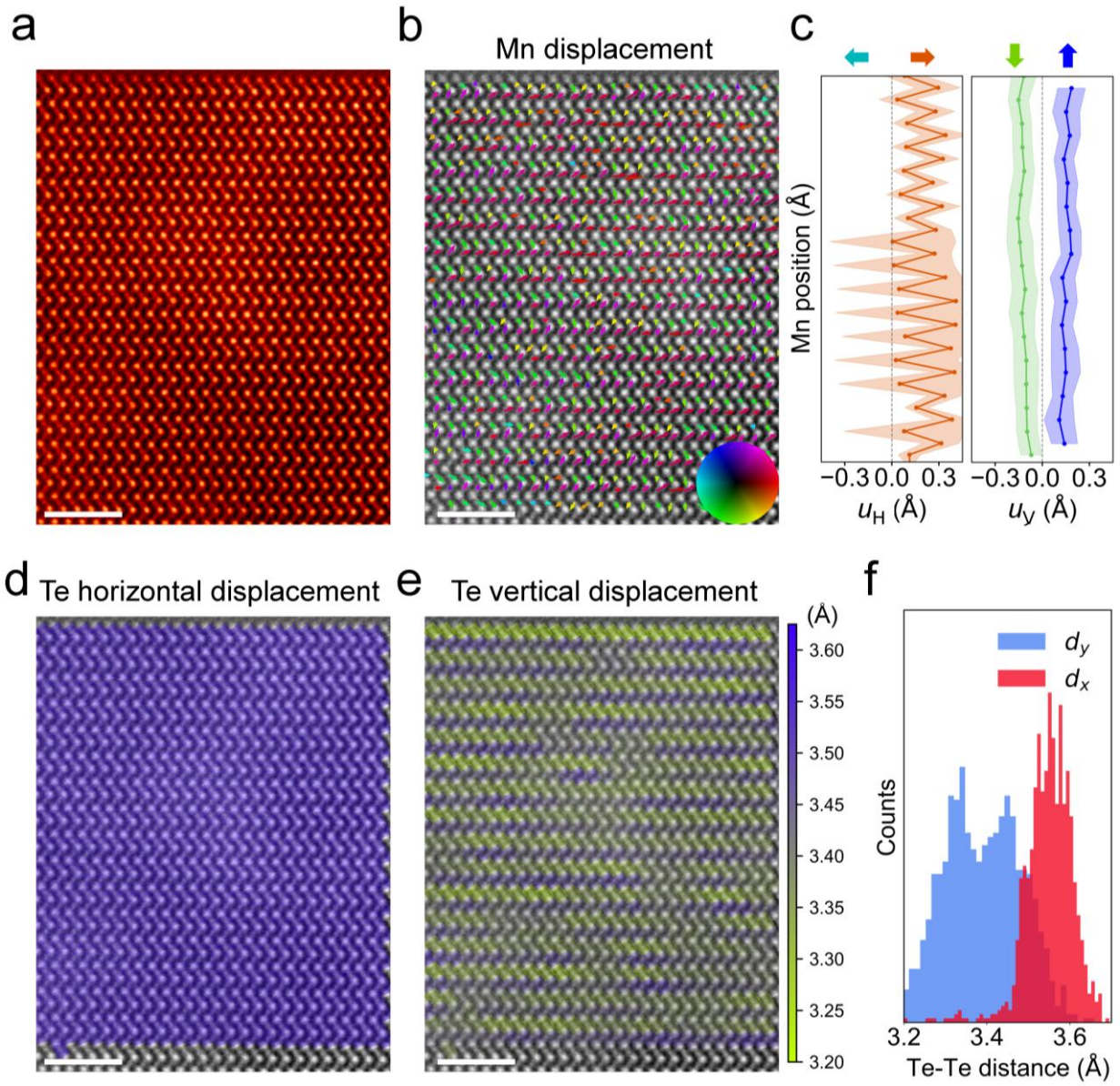


**Figure. S8 Atomic-scale observation of *Amm*2 lattice in α-MnTe thin film**. **(a).** A representative STEM-HAADF image showing the atomic structure of α-MnTe thin film along the *a*-axis. **(b).** Displacement vector map of the Mn sublattice. The vectors are calculated from the off-centering of Mn atomic columns relative to the centroid of the surrounding Te sublattice and are overlaid on the original HAADF image shown in **(a)**. **(c).** Statistical analysis of Mn-layer displacements, corresponding to the local structural motifs shown in **(a)**. Displacements of each Mn layer are resolved along the horizontal ($u_H$) and vertical ($u_V$) directions, respectively. Shaded regions in the plots indicate the corresponding standard deviations. **(d, e).** Nearest Te-Te distance mapping showing relatively uniform Te-Te spacing along the horizontal direction ($d_H$) in **(a)**, but modulated Te-Te spacing along the vertical direction ($d_V$) in **(e)**. **(f).** Histogram plot showing the distribution of Te–Te distances along the vertical ($d_V$) and horizontal ($d_H$) directions in the original HAADF image shown in **(a)**. Scale bars are 2 nm in **(a, b, d, e)**.

**Section 4. Symmetry breaking and distortion modes**

Group-theoretical analysis was employed to determine the symmetry-allowed subgroup distortions of the parent $P6_3/mmc$ α-MnTe structure. The observed structural motifs in STEM images can be considered as the combination of multiple distortion modes. Figure S9**a** demonstrates that the combined $\Gamma_2^-$ and $\Gamma_5^-$ modes lower the symmetry to $Cmc2_1$, whereas the combination of $\Gamma_4^-$ and $\Gamma_6^-$ mode results in $Amm2$ polar symmetry, as shown in Figure S9**b**. The coexistence of Mn and Te displacements further lowers the symmetry to $Cm$, as depicted in Figure S9**c-d**. To have a better visual comparison among different structures, all distorted lattices were oriented in the same coordinate system as the parent $P6_3/mmc$ α-MnTe structure.

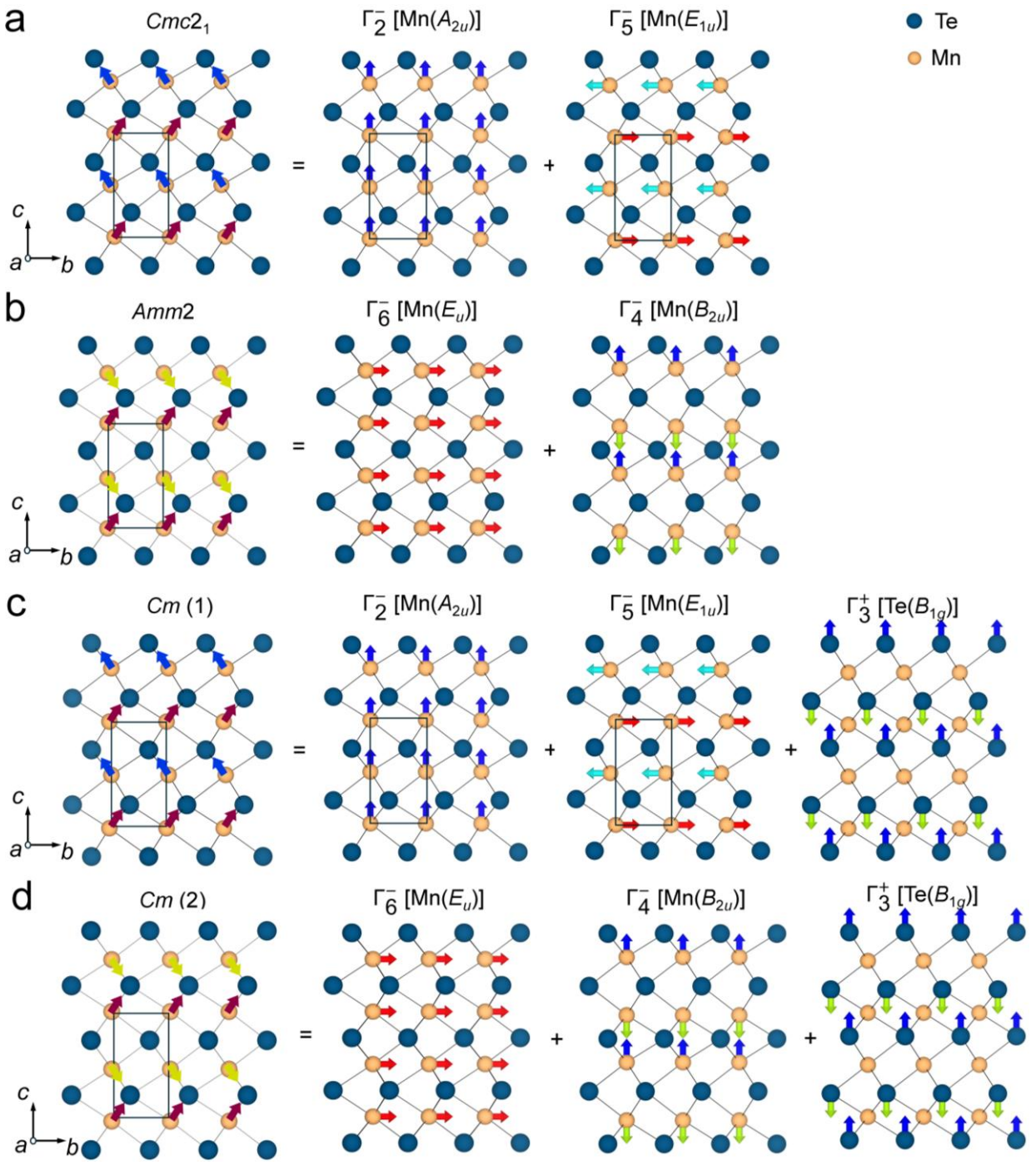


**Figure. S9 Atomic models of possible subgroup distortions allowed by the *P*6$_3$/*mmc* symmetry**. **(a).** The *Cmc*2$_1$-MnTe structure arising from combing the out-of-plane polar $\Gamma_2^-$ and in-plane antipolar $\Gamma_5^-$ modes. **(b).** The *Amm*2-MnTe polar structure arising from the combination of out-of-plane antipolar $\Gamma_4^-$ with the in-plane polar $\Gamma_6^-$ modes. **(c, d).** The coexisting Mn and Te displacements resulting in a lower symmetry *Cm*-MnTe structure.

**Section 5. PFM characterization of emergent ferroelectric order**

To investigate the ferroelectric order arising from inversion-symmetry-breaking distortions, we performed piezoresponse force microscopy (PFM) on a bulk α-MnTe crystal with the *c*-axis oriented nearly along the tip (Figure S10**a**). The α-MnTe was adhered by copper tape to a metal sample plate for grounding in the AFM. Given that the remanent polarization in α-MnTe originates predominantly from Mn displacements, the non-centrosymmetric $Cmc2_1$ or *Cm* lattices with out-of-plane polar displacements (along the $P6_3/mmc$ *c*-axis) are expected to yield the strongest ferroelectric response, while the *Amm*2 lattice, with in-plane polar displacements, should produce a much weaker response.

Figure S10**b-d** shows the representative topography, amplitude, and phase images acquired in the same scanning region. The phase image (Figure S10**d**) reveals distinct domains across the surface, with length scales generally larger than those resolved by STEM observation (around 10 ~ 20 nm). This discrepancy likely arises from the limited spatial resolution of the PFM probe (typically above 10 nm)[2]. We also show point spectra using switching spectroscopy PFM (SS-PFM). The details of PFM and SS-PFM measurements are described in *Methods*. Spectra acquired from the brighter phase contrast region, shown in Figure S10**e**, indicate the presence of amplitude hysteresis ("butterfly" loops) and phase hysteresis, characteristic of polarized domains. This region therefore likely corresponds to the $Cmc2_1$ or *Cm* polar lattices, which exhibit stronger polarization along the *c*-axis. In contrast, regions with low phase contrast (#2) exhibit almost no ferroelectric hysteresis (Figure S10**f**), suggesting that the *Amm*2 lattice with in-plane polar displacements may be the dominant structure in this region.

We note that these data are *consistent* with polarization characteristic of ferroelectric domains; however, PFM can be subject to "false positives" in certain cases[3]. The absence of hysteresis in certain domains (Figure S10**f**) does lend confidence that artifacts are minimized in this instance, though completely eliminating such effects requires other techniques, such as interferometric methods[4].

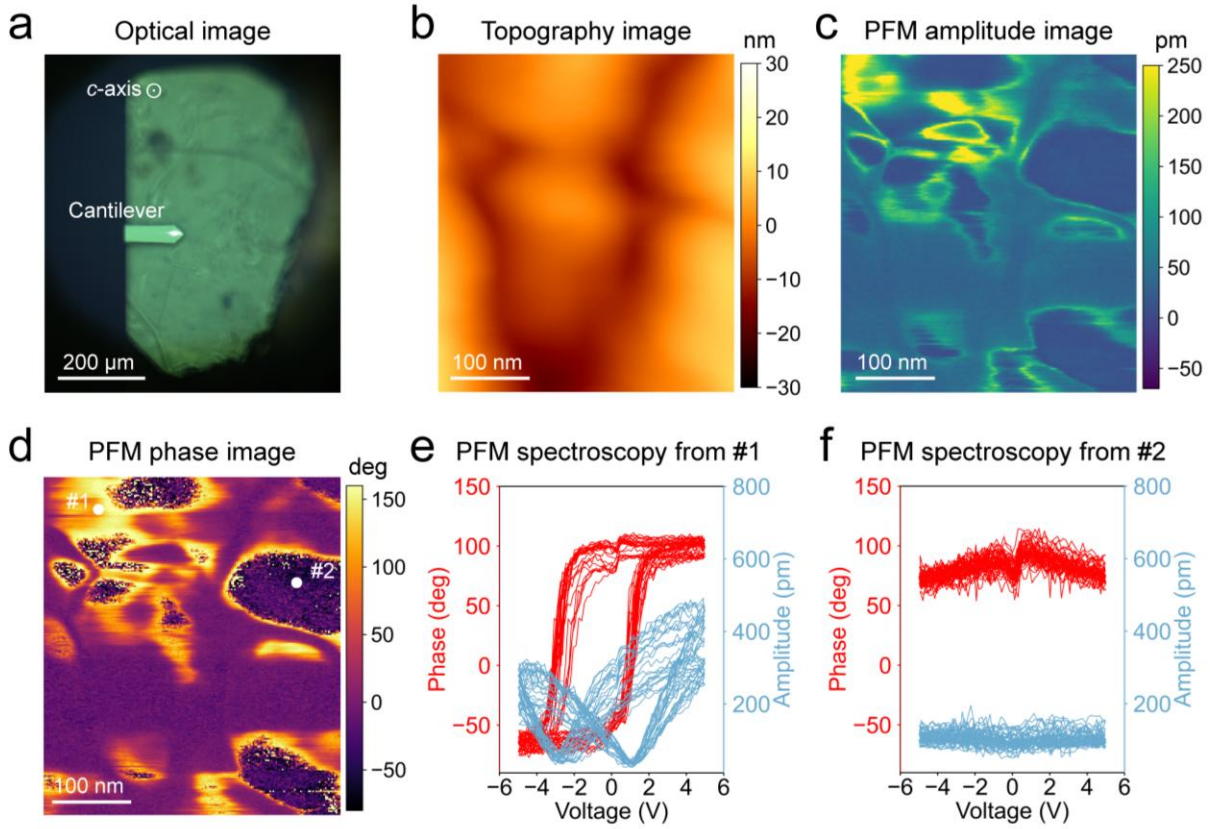


**Figure. S10 PFM measurement on a bulk α-MnTe crystal**. **(a).** Optical image showing the AFM cantilever position on α-MnTe crystal surface. **(b).** Representative surface topography image. **(c)** PFM amplitude image. **(d)**. PFM phase image of the local α-MnTe crystal. **(e).** Phase and amplitude measured by multi-cycle switching spectroscopy, demonstrating ferroelectric-like hysteresis on bare surface in region #1 labeled in **(d)**. **(f).** Phase- and amplitude-switching spectroscopy loops, showing no obvious ferroelectric-like hysteresis on bare surface in region #2 labeled in **(d)**.

## Section 6. DFT calculations on electronic band structures

The schematics shown in Figure S11 depict the opposite spin sublattices within each structural motif connected by the rotational operations. The lower-symmetry $Cmc2_1$ and $Amm2$ lattices exhibit non-relativistic spin symmetry operations $[C_2||C_2t_{1/2}]$ and $[C_2||C_2]$, respectively. In contrast, the opposite spin sublattices in the $Cm$ lattice cannot be interconverted by either a translation (or inversion) nor a rotation operation.

Without relativistic SOC, at $k_z = 0$ (use the $P6_3/mmc$ $k$-space coordinates as for all lattices), the spin degeneracy along the -$K$− $\Gamma$−$K$ nodal line is protected by the SSG symmetry operations for $P6_3/mmc$, $Amm2$ and $Cmc2_1$ lattices, as shown in Figure S11. While at $k_z \neq 0$, non-relativistic

spin splitting emerges along -$\overline{M}$–$\overline{\Gamma}$–$\overline{M}$ (Néel-vector easy axis), yet degeneracy is retained at $\overline{\Gamma}$. When altermagnetic symmetries are further broken in *Cm* lattice, besides having the non-relativistic spin splitting along both -$\overline{M}$–$\overline{\Gamma}$–$\overline{M}$ and -$K$–$\Gamma$–$K$, spin degeneracy is also lifted at $\Gamma$ and $\overline{\Gamma}$, indicating a mixed *d*-wave and *s*-wave state.

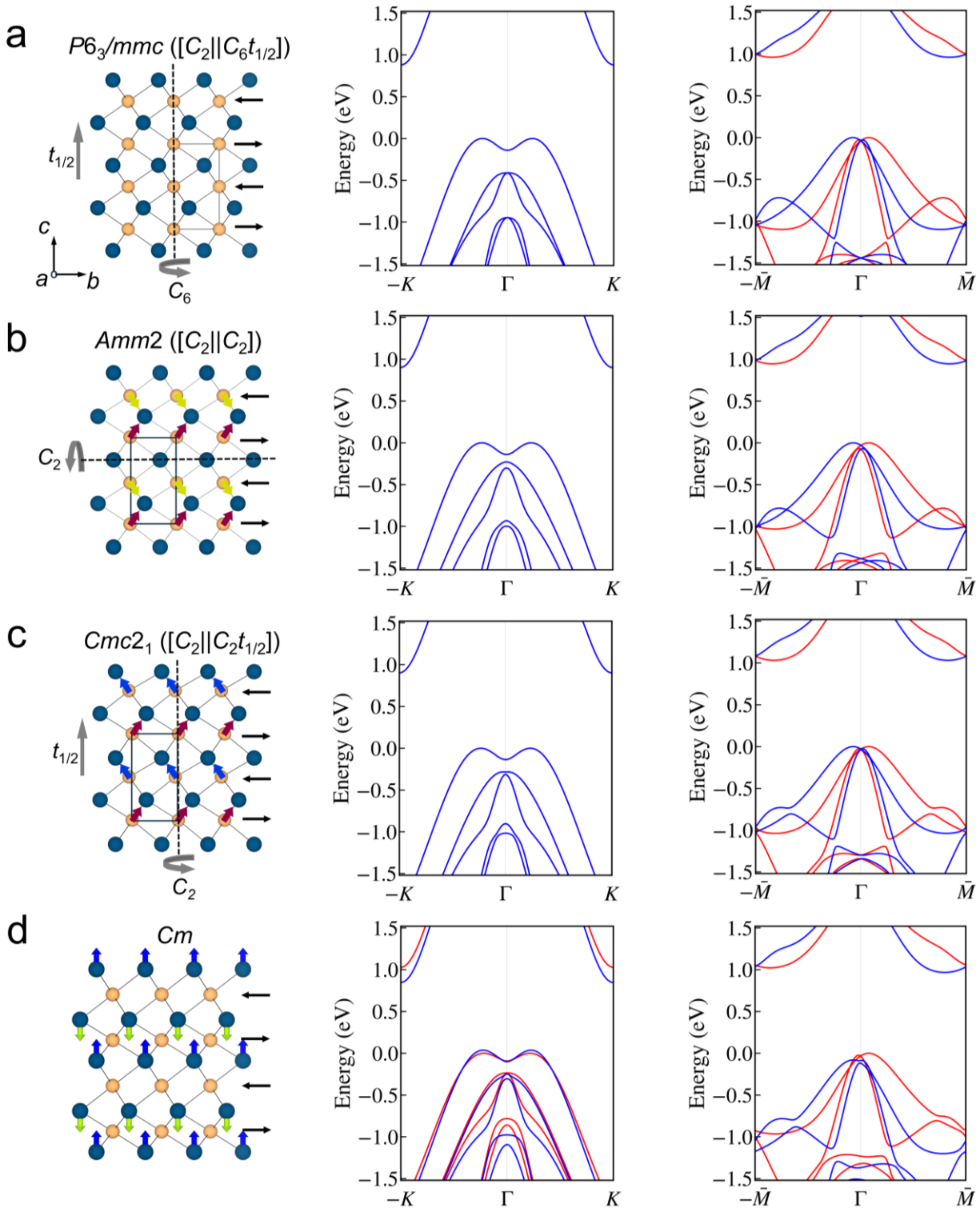


**Figure. S11 Electronic band structures of MnTe structures without SOC**. The spin-group generators of each structural motif are written in parentheses. The rotational operation connecting the opposite spin sublattices are labeled with dash lines. The alternating black arrows indicate the opposite spin moments across Mn sublattices. Blue and red colors mark opposite spin polarizations in band structure. Spin degeneracy is preserved along the -*K*–*Γ*–*K* nodal line, is lifted

along the -$\bar{M}$–$\bar{\Gamma}$–$\bar{M}$ path at $k_z \neq 0$ in **(a)** *P*6$_3$/*mmc*-MnTe, **(b)** *Amm*2-MnTe, **(c)** *Cmc*2$_1$-MnTn. With altermagnetic symmetry broken, *Cm*-MnTe lattice has momentum-dependent spin splitting along both -*K*–*Γ*–*K and* -$\bar{M}$–$\bar{\Gamma}$–$\bar{M}$ in **(d)**.

As shown in Figure S12, with SOC taken into account, the relativistic spin splitting occurs along both -$\bar{M}$–$\bar{\Gamma}$–$\bar{M}$ and -*K*–*Γ*–*K* in all lattices. Moreover, due to the interplay of broken inversion-symmetry and SOC, the spin-resolved band dispersions become asymmetric between positive and negative momenta in the noncentrosymmetric lattices.

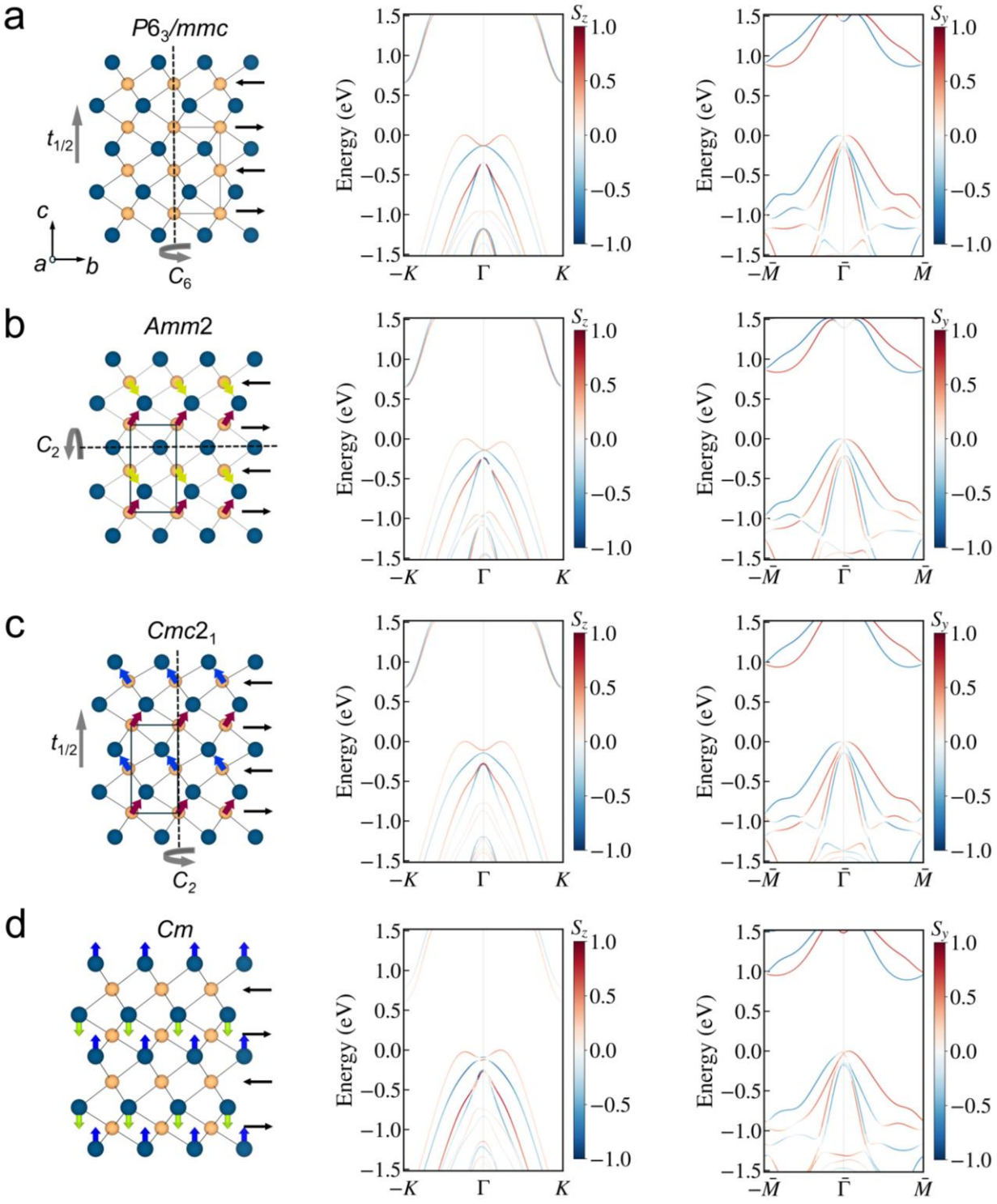


**Figure. S12 Electronic band structures of MnTe structures with SOC turned on**. The alternating black arrows indicate the opposite spin moments across Mn sublattices. The electronic band structures along -$\bar{M}$–$\bar{\Gamma}$–$\bar{M}$ as well as -*K*–*Γ*–*K*, showing the momentum-dependent spin splitting in **(a)** $P6_3/mmc$-MnTe, **(b)** *Amm*2-MnTe, **(c)** $Cmc2_1$-MnTe, as well as **(d)** *Cm*-MnTe lattice.

As demonstrated in Figure S13, when SOC is included, the spin groups of these three non-centrosymmetric lattices become ferromagnetic with canted magnetic moments, enabling a net magnetization along the out-of-plane direction (*c*-axis in parent $P6_3/mmc$ lattice).

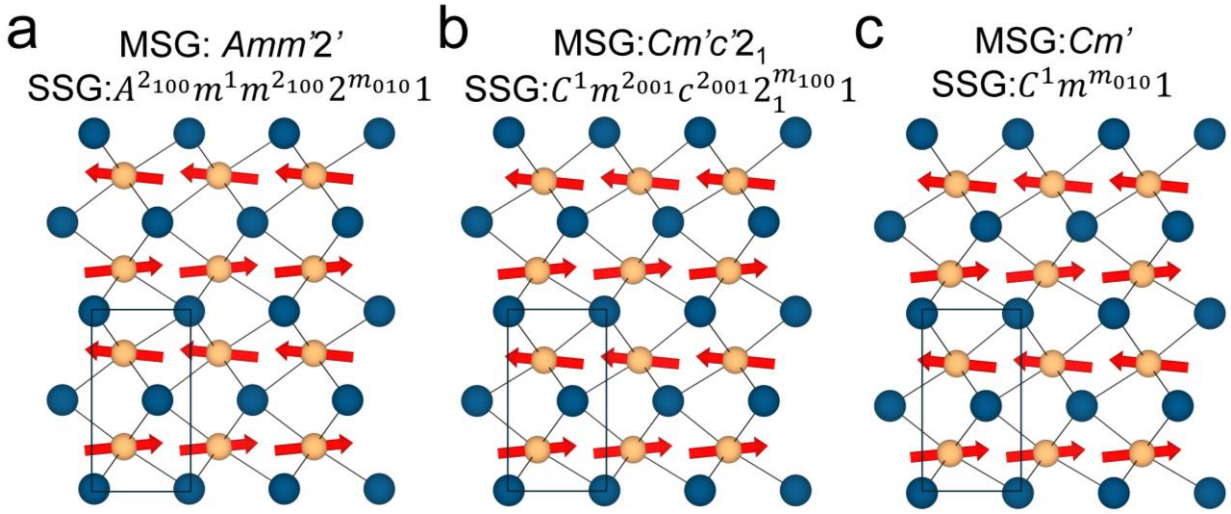


**Figure. S13 Symmetry-allowed magnetic orders of distorted structures**. With SOC, the relativistic magnetic-space-groups (MSG) allow for canted magnetic moments enabling net magnetism in non-centrosymmetric *Amm*2 in **(a)**, $Cmc2_1$ in **(b)** and *Cm* in **(c)**, respectively.

**Section 7. EMCD simulations**

The EMCD signal distributions in real space were calculated with magnetic spins oriented along the different crystallographic directions. Figure S14 displays calculation results for an 18-nm-thick sample projected along the *a*-axis. Here, we use the distorted lattice with *Cm* symmetry shown in Figure S14**a** as an example. For simplicity, we hypothetically consider all Mn atoms having the same magnetic moment of 1$\mu_B$ along *a*-, *b*-, or *c*-axis as illustrated schematically in Figure S14**b**-**d**. The positions of the Mn atomic columns are clearly resolved in the Mn $L_3$ energy-filtered image shown in Figure S14**e**. The zig-zag arrangement of Mn atomic columns arises from the atomic displacements of combined $\Gamma_2^-$ and $\Gamma_5^-$ modes.

In Figure S14**f-h**, when the magnetic moments are oriented along the *a*-axis—parallel to the electron beam—the EMCD signals appear but are relatively weak and noisy, hindering reliable detection and interpretation. In Figure S14**g**, with the magnetic moments lying in-plane along the

*b*-axis to the left, negative EMCD intensity is observed below the Mn atomic column, while positive intensity appears above it at the respective scan positions. For magnetic moments oriented upward along the *c*-axis, the EMCD signal exhibits negative intensity on the left side of the Mn column and positive intensity on the right side, as revealed in Figure S14**h**.

Our simulations show that EMCD signals in the distorted MnTe lattice are detectable, particularly when magnetic moments are perpendicular to the electron beam, and that their spatial distribution directly reflects the local moment orientation. We note that the antiferromagnetic ordering in the lattice would flip the sign of relevant features in every other Mn planes. Applying this to altermagnetic MnTe, where the $Mn_A$ and $Mn_B$ sublattices exhibit antiparallel magnetic moments within the *a*-*b* plane, we expect that the EMCD signal will exhibit alternating sign every two Mn planes and can be extracted from regions above or below each Mn column. We notice that a recent study by Song et al demonstrates similar EMCD analysis in antiferromagnets at the atomic scale[5].

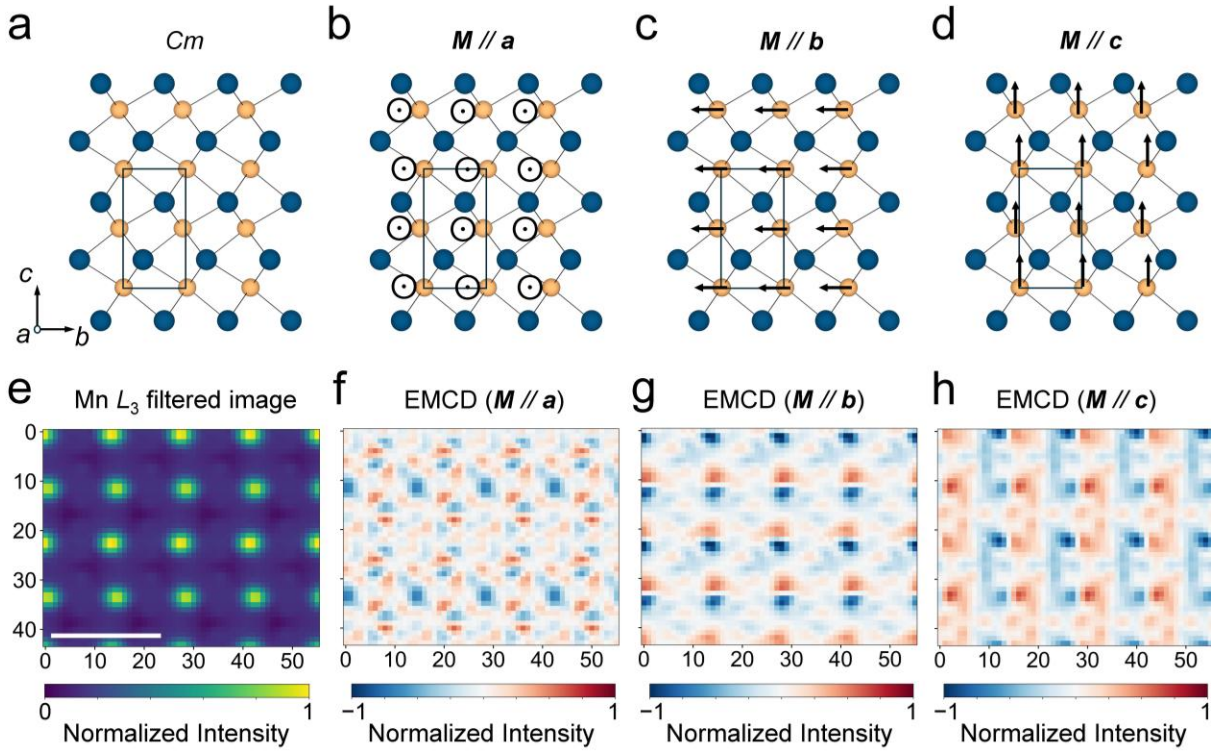


**Figure. S14 Spatial distribution of EMCD signals depending on the magnetic moment orientation**. **(a).** Atomic models of *Cm* lattice showing the combined $\Gamma_2^-$ and $\Gamma_5^-$ modes. **(b-d).**

Atomic models of *Cm* lattice with magnetic moment aligning along *a*-, *b*-, and *c*-axis, respectively. **(e).** Mn $L_3$ energy-filtered image showing the Mn column with normalized intensity. Scale bar is 0.5 Å. **(f-h).** Real space distribution of EMCD signals at Mn $L_3$ edge with magnetic moment oriented along *a*-, *b*-, and *c*-axis, respectively. The EMCD signals can be distinguished by extracting signals from different regions in the neighborhood of the atomic column. Displayed intensities are normalized to the maximum value.

## Section 8. Atomic-scale EMCD measurements

To probe the magnetic order in local MnTe lattice, we acquired atomically resolved EELS spectra to detect magnetic circular dichroism signals at the Mn $L_{2,3}$ edge. The scanning area for the local structural motifs was 5 nm × 5 nm field of view with 180 × 180 pixels (the spectra were cropped to avoid the edge area). To enhance the signal-noise-ratio, template-matching was applied to obtain the average spectra image as shown in Figure S15.

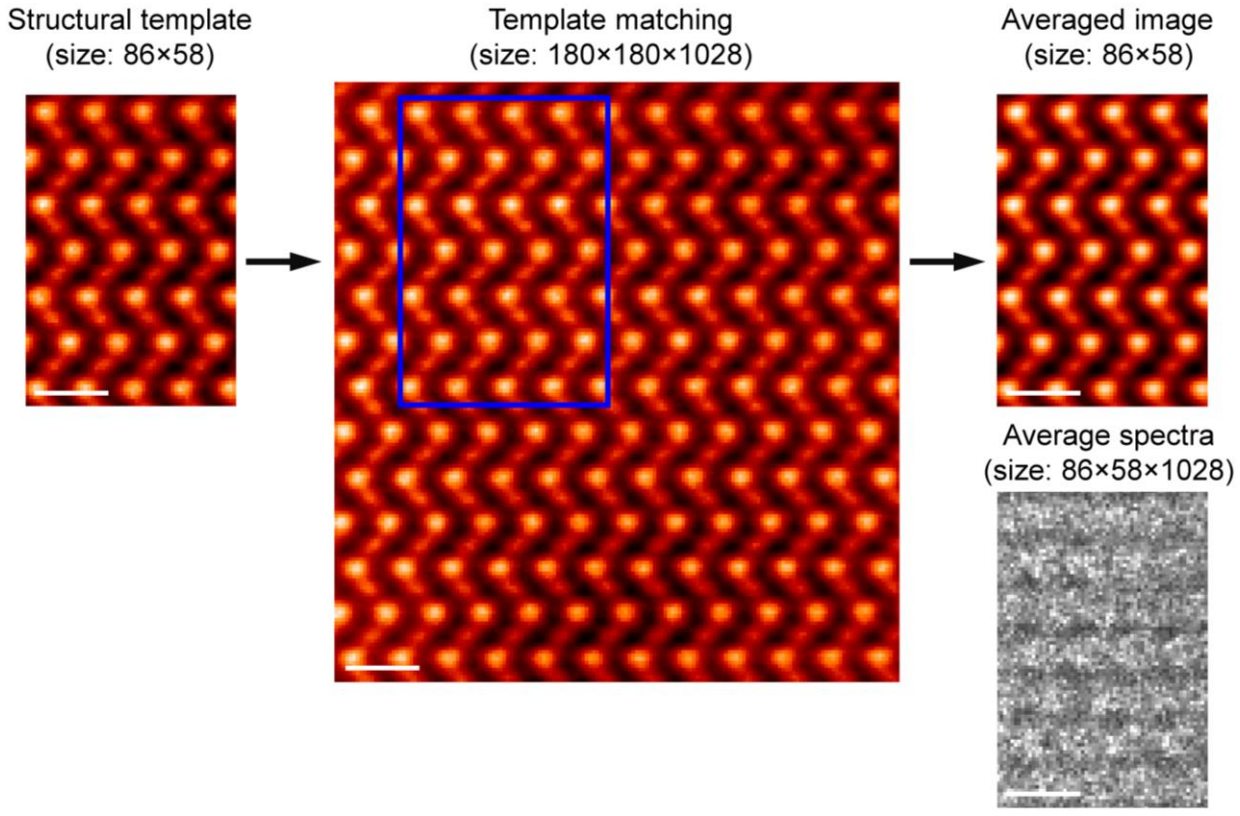


**Figure. S15 Average spectra image obtained by applying template matching**. The local structural image was selected as the template. The average spectra were obtained for post-processing. Scale bars are 0.5 nm.

As shown in Figure S16**a**, the positions of Mn and Te atomic columns were identified from the average structural image using 2D Gaussian fitting. Layer-resolved EELS signals were then extracted from each Mn sublattice using a horizontal mask offset by 2-3 pixels from the Mn peak positions (Figure S16**b**). The averaged Mn $L_{2,3}$ spectrum ($<\sum(Mn_A+Mn_B)>$) were obtained over all Mn layers. The power-law fitting was applied for background subtraction as shown in Figure S16**c-d**. The post-edge normalization was performed after background subtraction as shown in Figure S16**e**. The magnetic EMCD signals can be obtained by calculating the dichroism between the layer-resolved Mn $L_{2,3}$ spectra of $Mn_A$ and $Mn_B$ sublattices and the averaged Mn $L_{2,3}$ spectrum ($<\sum(Mn_A+Mn_B)>$) over all Mn layers.

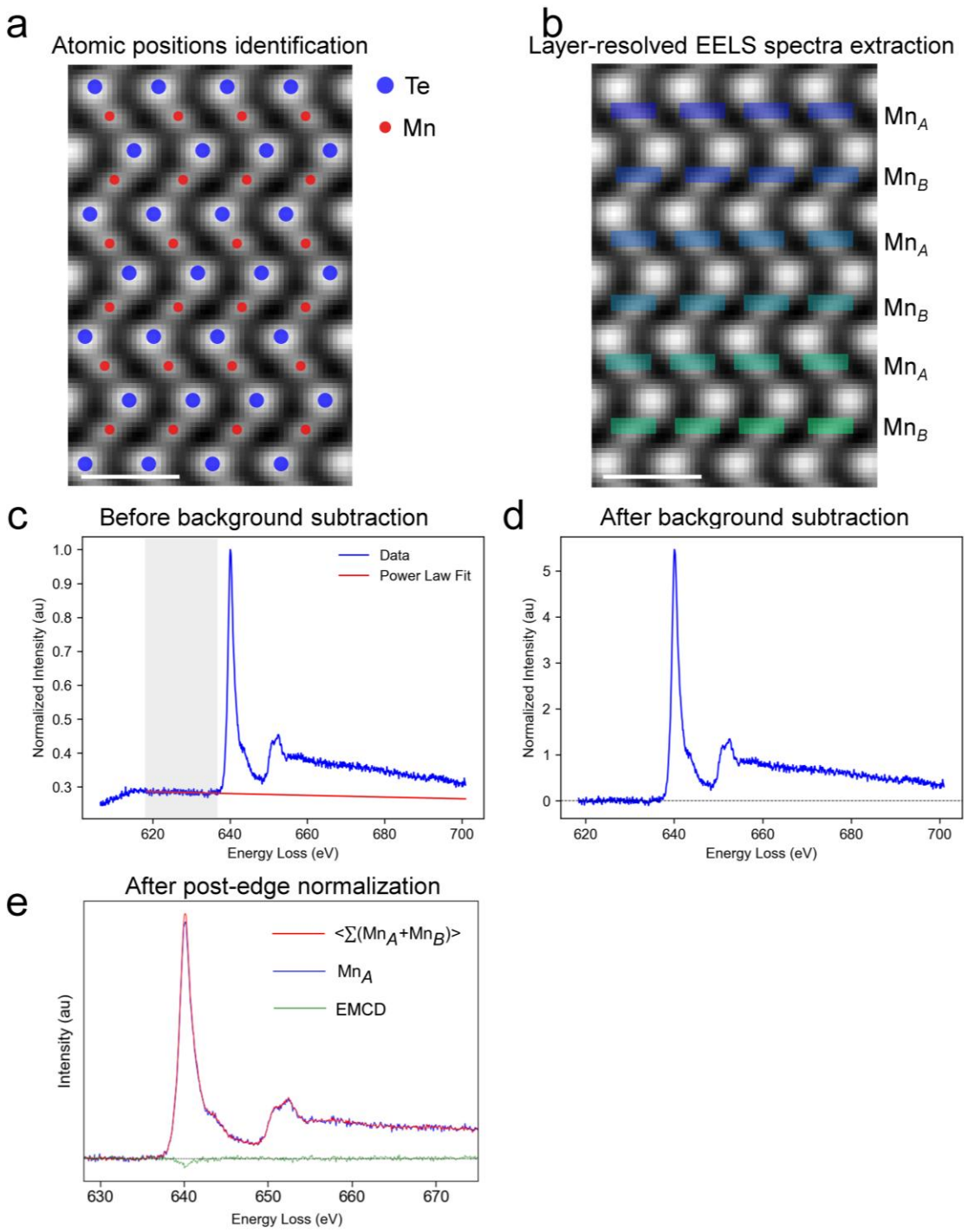


**Figure. S16 EELS data processing**. **(a).** The identification of atomic columns in the averaged structural image. **(b).** Layer-resolved EELS extraction with horizontal mask (3 pixels in height and 5-7 pixels in width). **(c-d).** The background subtraction by power-law fitting. The shaded area indicates the energy range of the fitting window. **(e).** The post-edge normalization for EMCD calculation. Scale bars are 0.5 nm in **(a-b)**.

Following the guidance of our EMCD simulations, we extracted EMCD signals from local *Cmc*2$_1$-MnTe lattice in regions above and below the Mn column. Figure S17**a** reveals clear alternating EMCD signals at $L_3$ edge across the $Mn_A$ and $Mn_B$ sublattices when signals are extracted from above the Mn column. These plots correspond to those presented in Figure 3**e** of the main text. In Figure S17**b**, when signals are extracted from below the Mn column, alternating EMCD signals at the $L_3$ edge are still observed across the $Mn_A$ and $Mn_B$ sublattices. However, the sign of the EMCD signal flips at each Mn sublattice compared to the plots in Figure S17**a**. Our experimental EMCD measurements thus confirm altermagnetic ordering in the *Cmc*2$_1$-MnTe lattice.

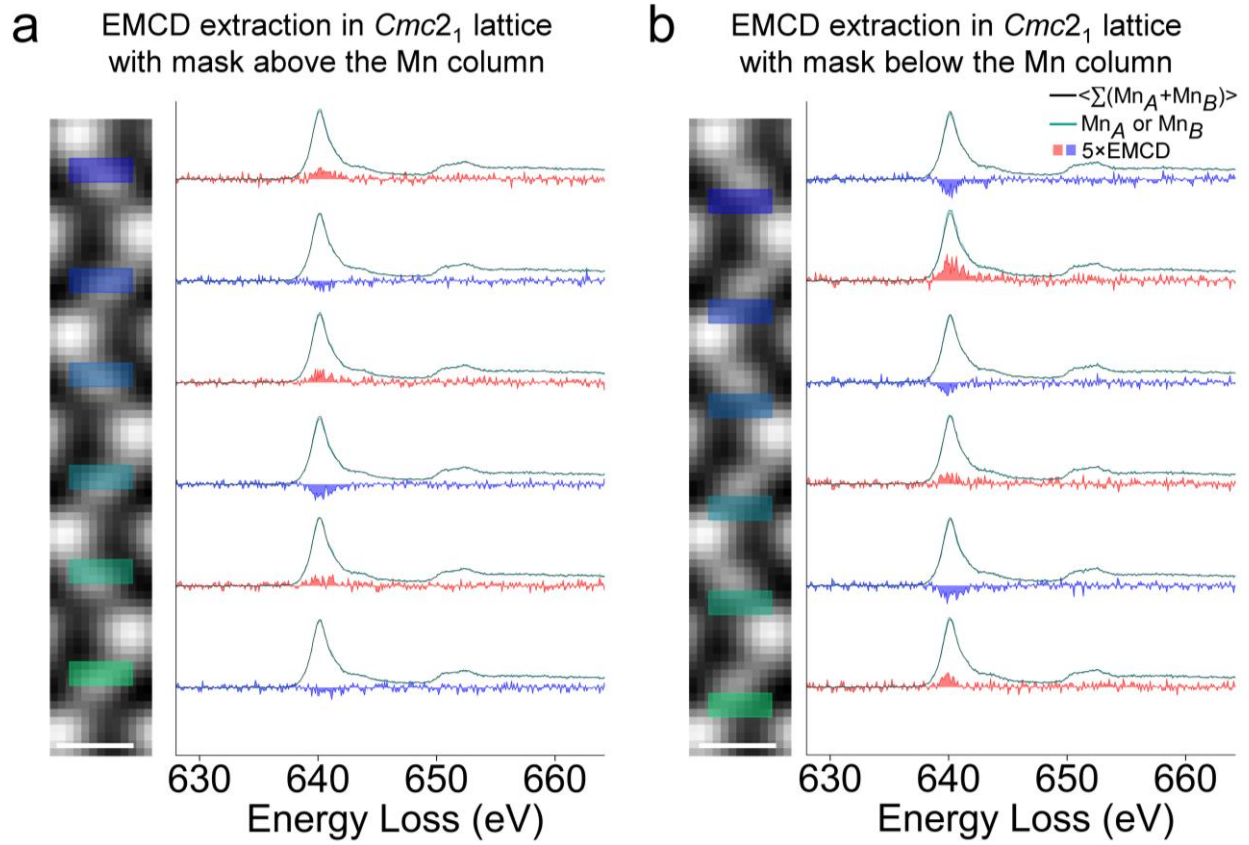


**Figure. S17 EMCD signals extraction in local *Cmc*2$_1$-MnTe lattice**. **(a).** EMCD signals extraction in regions above the Mn column. The same EMCD plots are reproduced in Figure 3**e** of the main text. **(b).** EMCD signals extracted from regions below the Mn column. For each Mn sublattice, the EMCD signal sign is inverted between regions above and below the Mn column. Scale bars are 0.25 nm in **(a-b)**.

A similar EMCD analysis was performed for local *Amm*2-MnTe lattice, focusing on regions above and below the Mn column. Figure S18**a** reveals clear alternating EMCD signals at $L_3$ edge across the $Mn_A$ and $Mn_B$ sublattices when signals are extracted from above the Mn column. These plots are reproduced in Figure 3**f** of the main text. When signals are extracted from below the column (Figure S18**b**), alternating EMCD signals are still observed, but the sign flips at each Mn sublattice relative to Figure S18**a**. Therefore, our experimental EMCD measurements also confirm altermagnetic ordering in the *Amm*2-MnTe lattice.

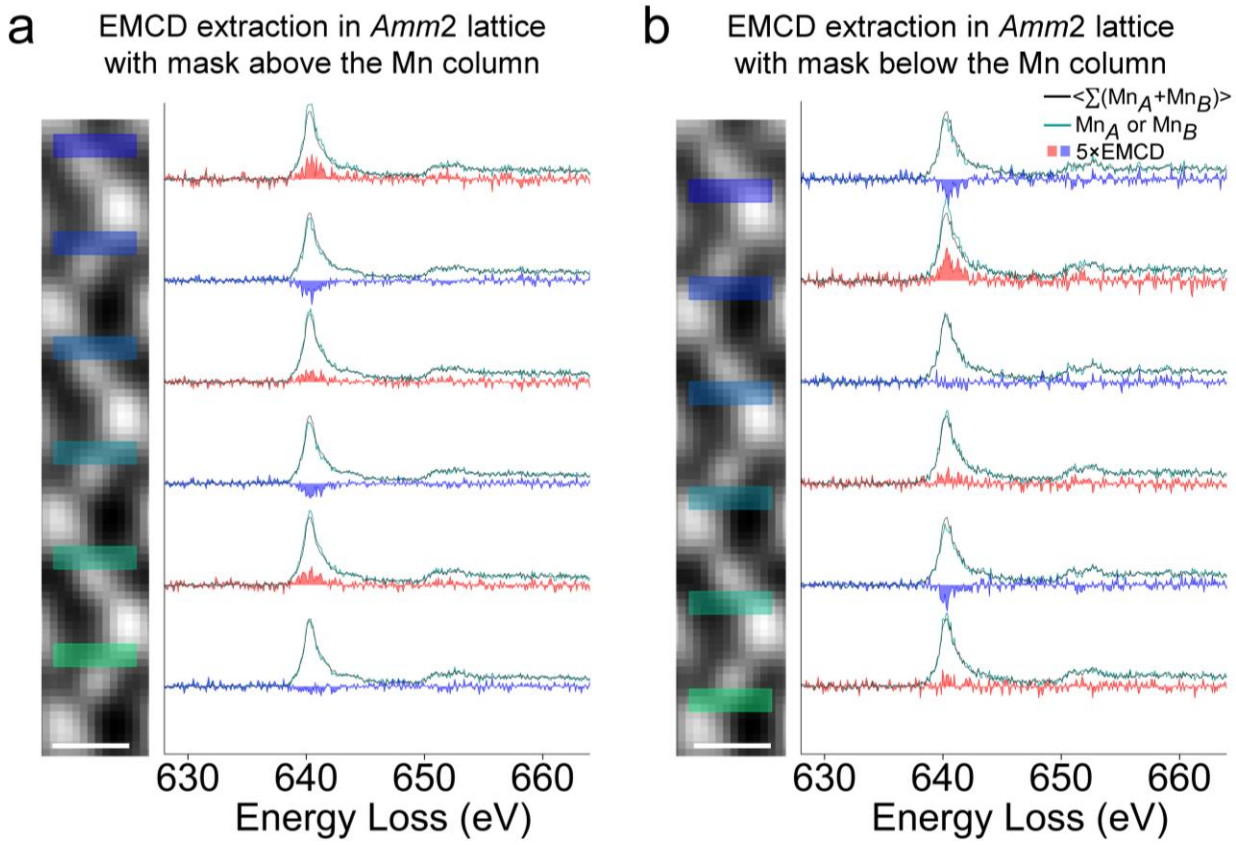


**Figure. S18 EMCD signals extraction in local *Amm*2-MnTe lattice**. **(a).** EMCD signals extraction in regions above the Mn column. The same EMCD plots are reproduced in Figure 3**f** of the main text. **(b).** EMCD signals extracted from regions below the Mn column. For each Mn sublattice, the EMCD signal sign is inverted between regions above and below the Mn column. Scale bars are 0.25 nm in **(a-b)**.

**Section 9. MnTe heterostructure**

Figure S19**a** reveals the presence of multiple narrow structural impurities embedded in the α-MnTe lattice. These structural impurities show higher *Z*-contrast implying the possible enrichment of heavy elements. While they extend laterally over tens of nanometers, their vertical dimension is limited to a half-unit-cell (~0.35 nm). Core-loss EELS measurements in Figure S20 indicate that the structural impurities are relatively depleted in Mn and relatively enriched in Te compared with the surrounding α-MnTe lattice.

Figure S19**b** shows the quantitative Mn displacement vectors across the entire region shown in Figure S19**a**, revealing three dominant distortion patterns associated with the Mn displacements (see Figure S21 below). In the bottom portion of the image, the Mn atoms undergo combined distortion modes corresponding to a *Amm*2-MnTe lattice; in the top-left region, the Mn displacements correspond to a *Cmc*2$_1$-MnTe lattice; while in the top-right region, the Mn atoms display enhanced horizontal displacements corresponding to the $\Gamma_6^-$ mode. Similar to the pristine α-MnTe lattice in Figure 2, the Te–Te spacing along the *b*-axis ($d_H$) remains relatively uniform as shown in Figure S19**c**. The Te sublattice displacements along the *c*-axis ($d_V$) are quantified in Figure S19**d**. The presence of half-unit-cell structural impurity induces significant vertical tensile strain to the α-MnTe lattice in the top-right region. This vertical strain strongly influences the horizontal displacements of Mn atoms, suggesting that local inversion-breaking structural motifs in α-MnTe may be tunable by strain.

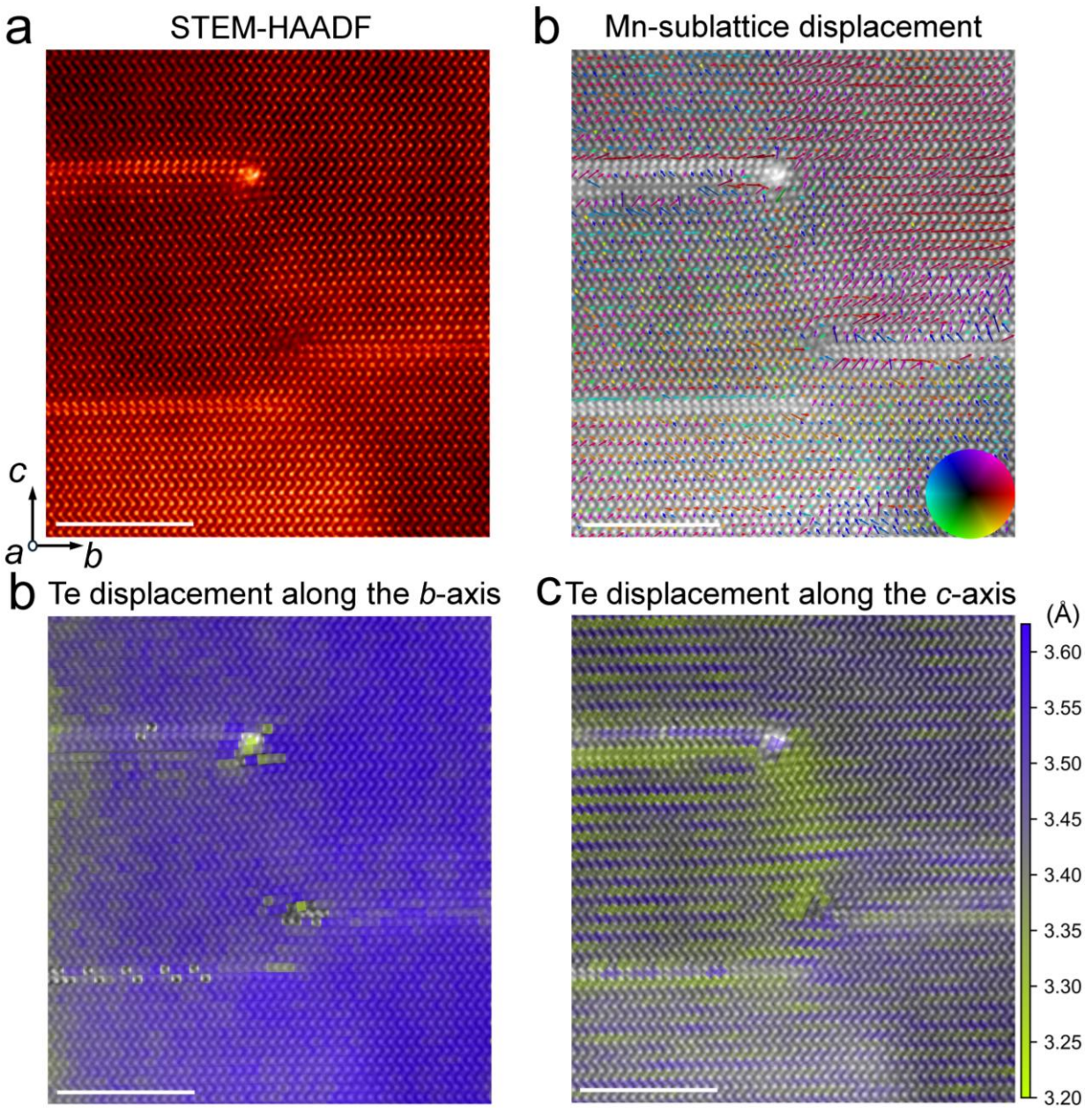


**Figure. S19 Structural distortions across MnTe heterostructures**. **(a).** A representative STEM–HAADF image of MnTe heterostructures viewed along the *a*-axis, revealing the atomic structure of a half-unit-cell impurity phase, which appears with brighter contrast. **(b).** Displacement vector map of the Mn sublattice. The vectors are calculated from the offset of Mn atomic columns relative to the centroid of the surrounding Te sublattice and are overlaid on the original HAADF image shown in **(a)**. **(c-d).** Nearest-neighbor Te–Te distance map along the horizontal direction ($d_H$) and vertical direction ($d_V$) in the original HAADF image shown in **(a)**, which reflect the Te-sublattice displacements along the *b*-axis and *c*-axis, respectively. A pronounced strain field is clearly visible around the half–unit-cell impurity lattices. Scale bars are 5 nm in **(a-d**).

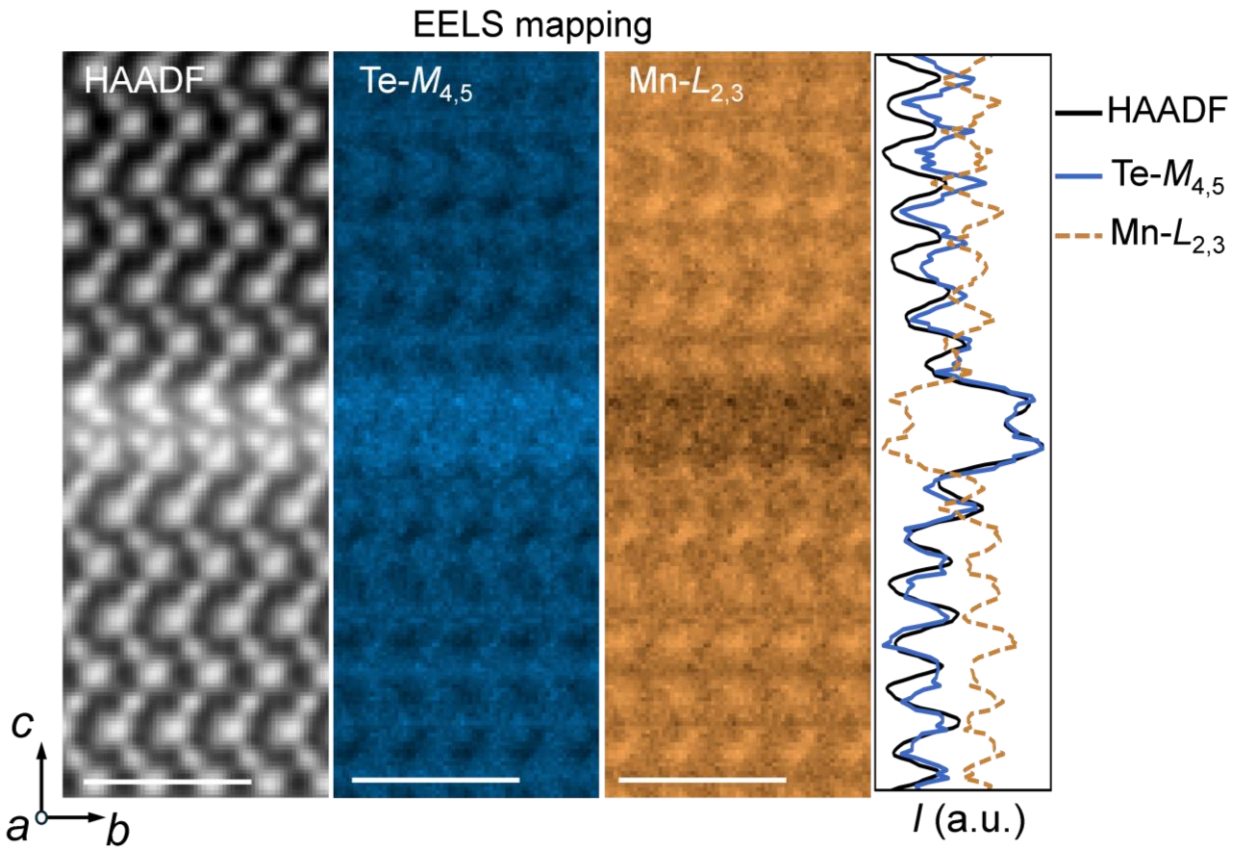


**Figure. S20 Core-loss EELS mapping across the MnTe heterostructure.** *Z*-contrast variation and integrated EELS signals confirm the enrichment of heavy Te atom inside the half-unit-cell structural impurity. Scale bars are 0.5 nm.

From quantitative analysis of the STEM-HAADF image in Figure S21**a**, we identify three distinct distortion domains arising from Mn displacements (Figures S21**b**–**d**). The structural domain located in the top-right region displays enhanced Mn displacements along horizontal direction corresponding to the $\Gamma_6^-$ mode as shown in Figure 21**c**. This structural domain is strongly affected by the vertical strain field imposed by the half-unit-cell structural impurity, implying the plausible tunability of polar order in α-MnTe through strain engineering.

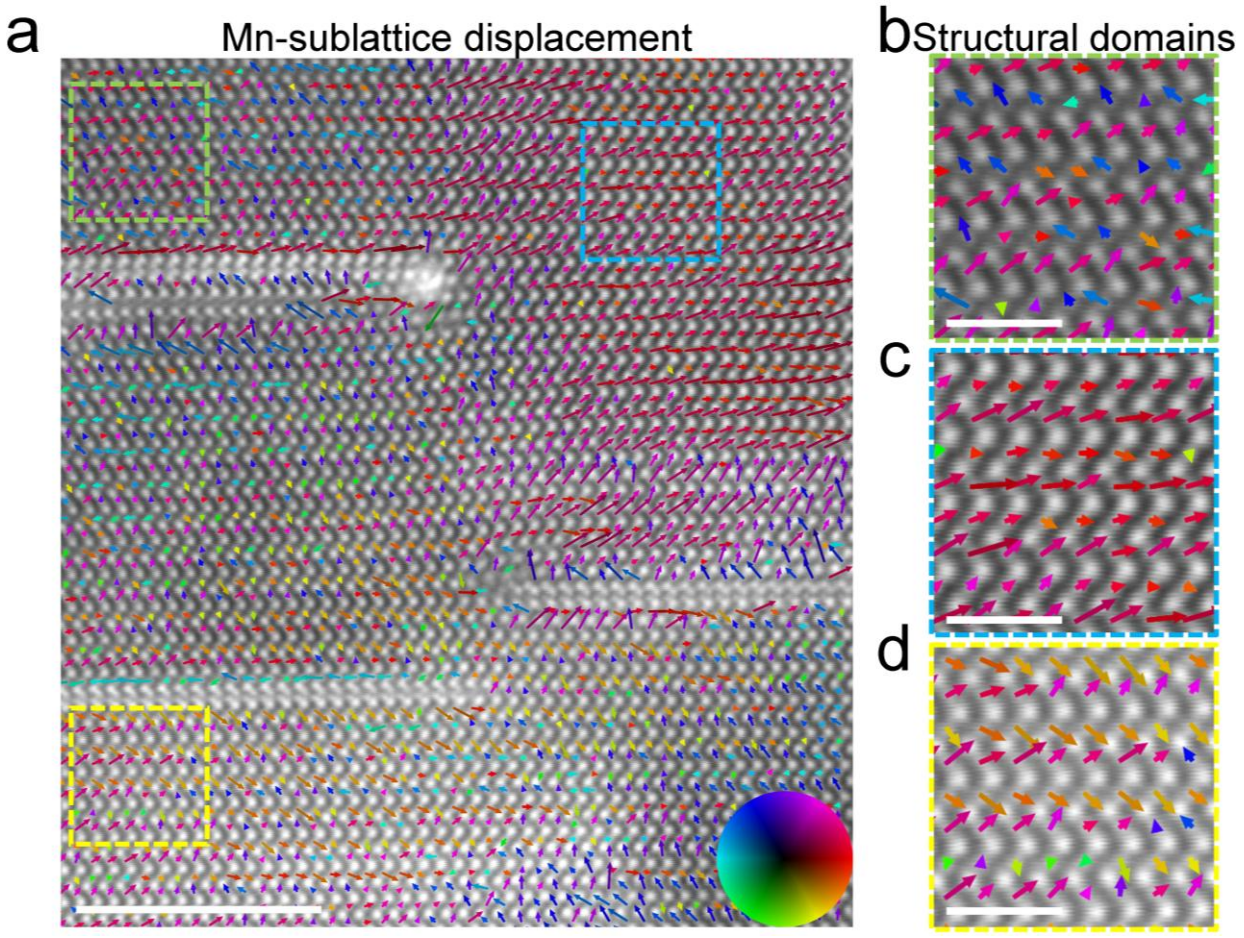


**Figure. S21 Structural domains around the MnTe heterostructures. (a).** Displacement vector map of the Mn sublattice. The vectors are calculated from the offset of Mn atomic columns relative to the centroid of the surrounding Te sublattice and are overlaid on the original HAADF image. **(b-d).** Three structural domains were extracted and zoomed in for a better visualization. Scale bars are 5 nm in **(a)** and 1 nm in **(b-d)**.

We performed systematic searches for all the possible MnTe structural polymorphs matching the atomic configuration shown in the half-unit-cell impurity. As illustrated in Figure S22, a half-unit-cell of monoclinic $P2_1/m$ phase (MC), when projected along the [110] direction (Figure S20**a**), best reproduces the atomic configuration of the structural impurities observed in STEM-HAADF image. For the heterostructure with coherent interface as illustrated in Figure S22**b**, half-unit-cell MC structure possesses a higher Te density but lower Mn density along the columns relative to the surrounding α-MnTe lattice. This variation in atomic density gives rise to the brighter *Z*-contrast in STEM-HAADF imaging and Te enrichment as observed in elemental mapping.

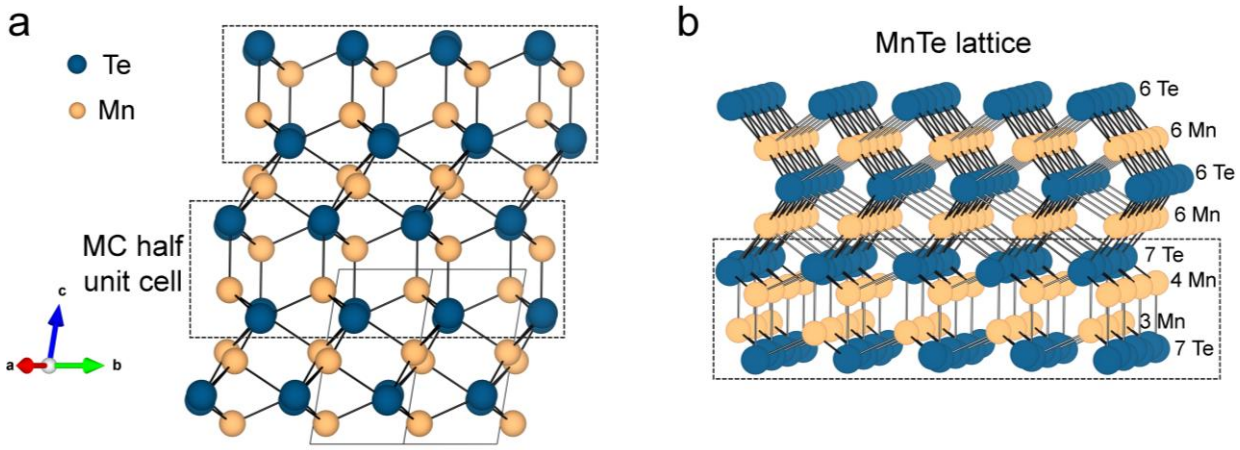


**Figure. S22 Atomic model of MnTe heterostructures. (a).** Structural model of the monoclinic $P2_1/m$ phase (MC), viewed along the [110] direction. The half-unit-cell of MC phase showing the same atomic configuration with STEM-HAADF image is enclosed by dash boxes. **(b).** Atomic model of the MnTe heterostructure with coherent interface. The half-unit-cell MC region exhibits a higher Te column density but lower Mn column density relative to the adjacent α-MnTe lattice.

Figure S23**a** depicts a structural model of MnTe heterostructure consisting of α-MnTe with an embedded half-unit-cell MC lattice. The simulated STEM image shown in Figure S23**b** demonstrates a good agreement with the experimental image in terms of both atomic arrangement and contrast variation.

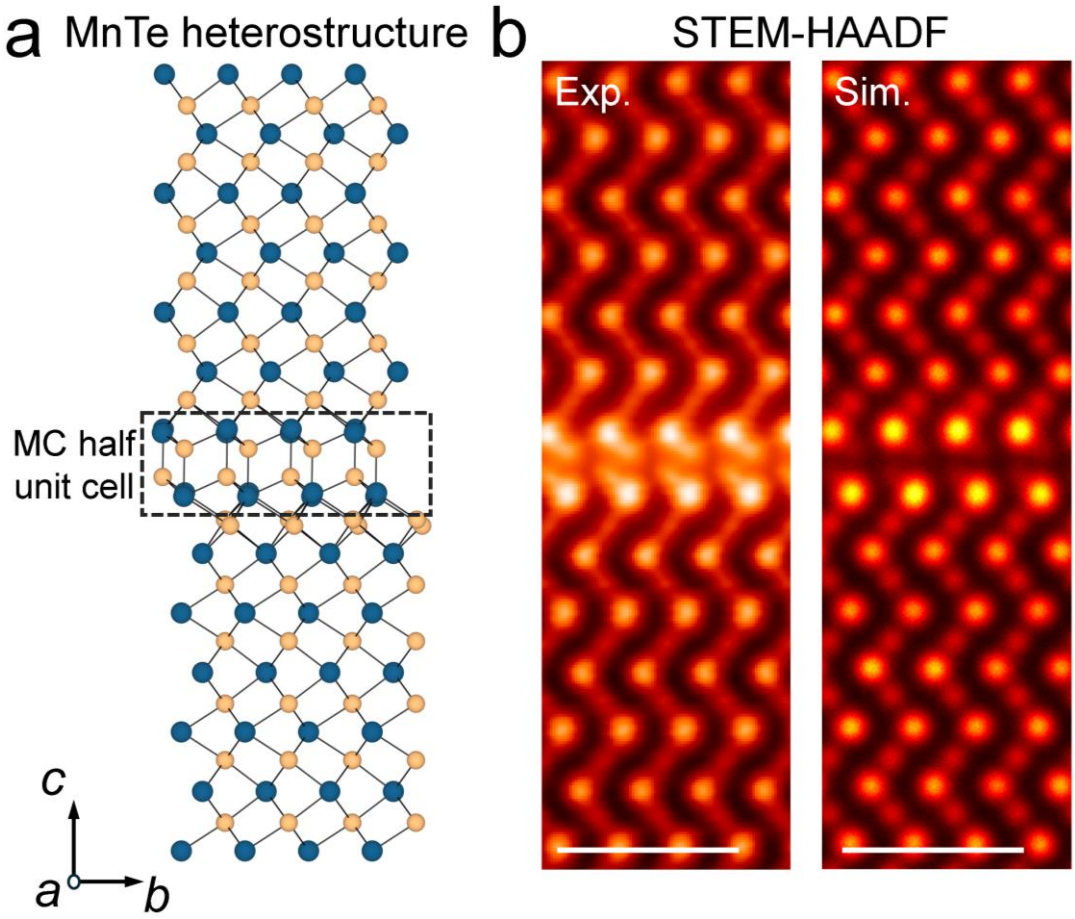


**Figure. S23 Atomic imaging of MnTe heterostructure. (a).** Atomic model depicting the MnTe heterostructure composed of α-MnTe with a half–unit-cell MC lattice embedded in the middle, enclosed by blue dashed lines. **(b).** Experimental and simulated STEM-HAADF images of the MnTe heterostructure. Scale bars are 1 nm in **(b)**.

As shown in Figure S24, we performed EMCD measurements to probe the magnetic order of the local structure across the half-unit-cell MC impurity. For the Mn sublattices away from the MC impurity, EMCD spectra still exhibit clear alternating dichroic signals at $L_3$ edge (above the MC lattice). However, this alternating pattern is disrupted for the Mn layers adjacent to the half-unit-cell MC impurity (below the MC lattice). This disruption indicates that the MC impurity and its associated strain field perturb the local magnetic contrast, although the precise mechanism, whether structural, magnetic, or scattering-related, remains to be clarified.

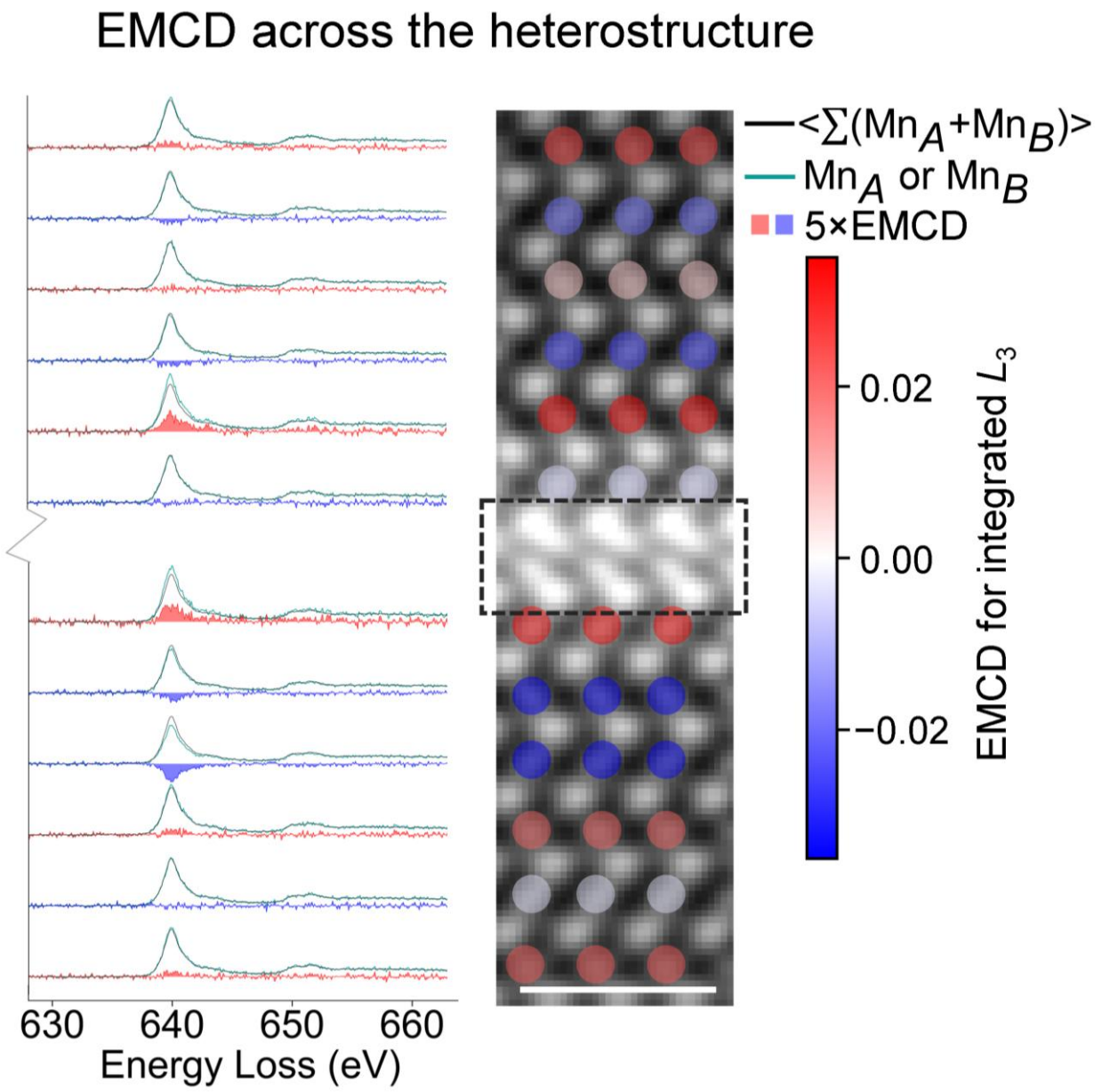


**Figure. S24 Magnetic order across MnTe heterostructure**. **Left panel:** Layer-resolved EELS spectra focusing on Mn-$L_{2,3}$ edges, acquired across the MnTe heterostructure. The EMCD signals were obtained by taking the difference between the layer-resolved EELS spectra (in green) and the average EELS spectrum (in black) over Mn layers excluding those within the MC half–unit-cell region. All spectra shown are background-subtracted and post-edge normalized. **Right panel:** The color and intensity of the circles schematically represent the strength of the EMCD signal at the Mn $L_3$ edge for each atomic row. Scale bars is 1 nm.

**Section 10. In-situ heating STEM measurements**

To explore the possible origin of the structural distortions in α-MnTe, such as spin-lattice coupling, we performed in situ heating STEM experiments. As shown in Figure S25**a**, we prepared the TEM lamella using FIB milling and transferred onto a heating chip, positioned over the empty hole. TEM image in Figure S25**b** indicates the prepared STEM specimen has enough transparent area over the hole region for atomically resolved STEM imaging.

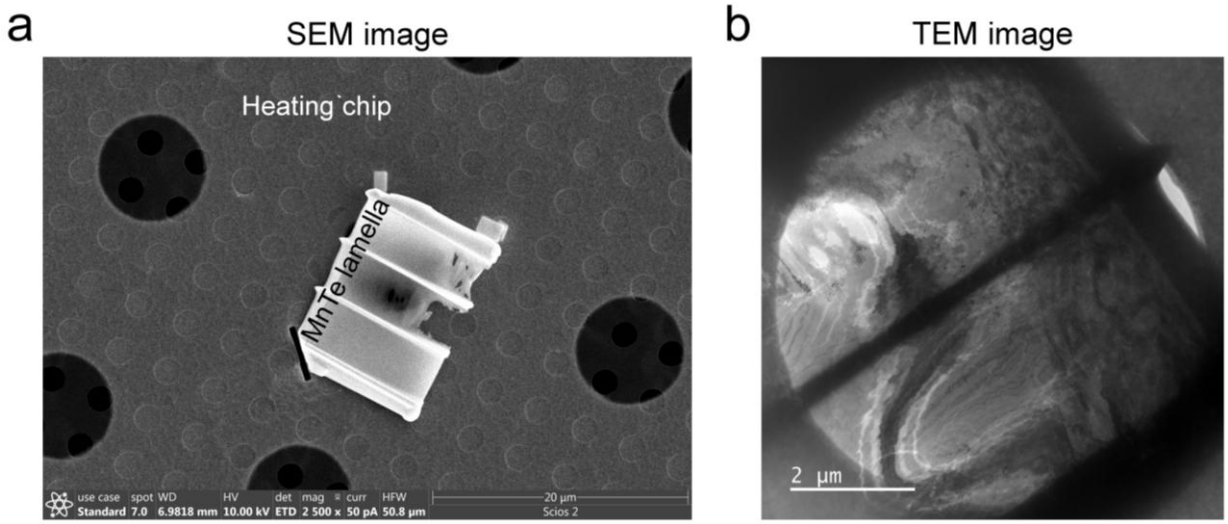


**Figure. S25 α-MnTe specimen for in-situ heating experiments. (a).** Scanning electron microscopy (SEM) image showing the α-MnTe specimen mounted on a heating chip. **(b).** TEM image showing the transparent area of α-MnTe specimen over the hole.

We first examined the α-MnTe lattice structure using STEM-HAADF imaging at room temperature. Figure S26 shows the quantified Mn and Te displacements in a local region of the α-MnTe specimen on a heating chip. In Figure S26**b**, consistent with the Mn displacement patterns observed in other samples, the same distortion modes—including those corresponding to $Cmc2_1$ and $Amm2$ symmetries—are readily identified. Similarly, the $\Gamma_3^+$ distortion mode, reflecting Te displacements along the *c*-axis, is also observed in Figure S26**c**.

In situ STEM measurements were conducted to capture changes in lattice symmetry above the Néel temperature. The α-MnTe specimen was heated on the chip up to 100 °C at a controlled rate of 30 °C/min. STEM imaging began after holding the specimen at the target temperature for 30 minutes. Figure S27**a** shows the atomically resolved lattice structure in a local region at 100 °C. We should note that this region differs from the one recorded in Figure S26**a** at room

temperature due to the thermal drift during the heating process. Figure S27**b** presents the quantitative Mn displacement vectors across the entire region. Obviously, the symmetry breaking lattice distortions from Mn sublattice still exist at high temperature. Te displacements along the *c*-axis corresponding to the $\Gamma_3^+$ mode were also captured in Figure S27**c-d**. Therefore, these distortions are not driven by magnetic ordering, indicating that mechanisms other than spin-lattice coupling should be responsible and require further investigation.

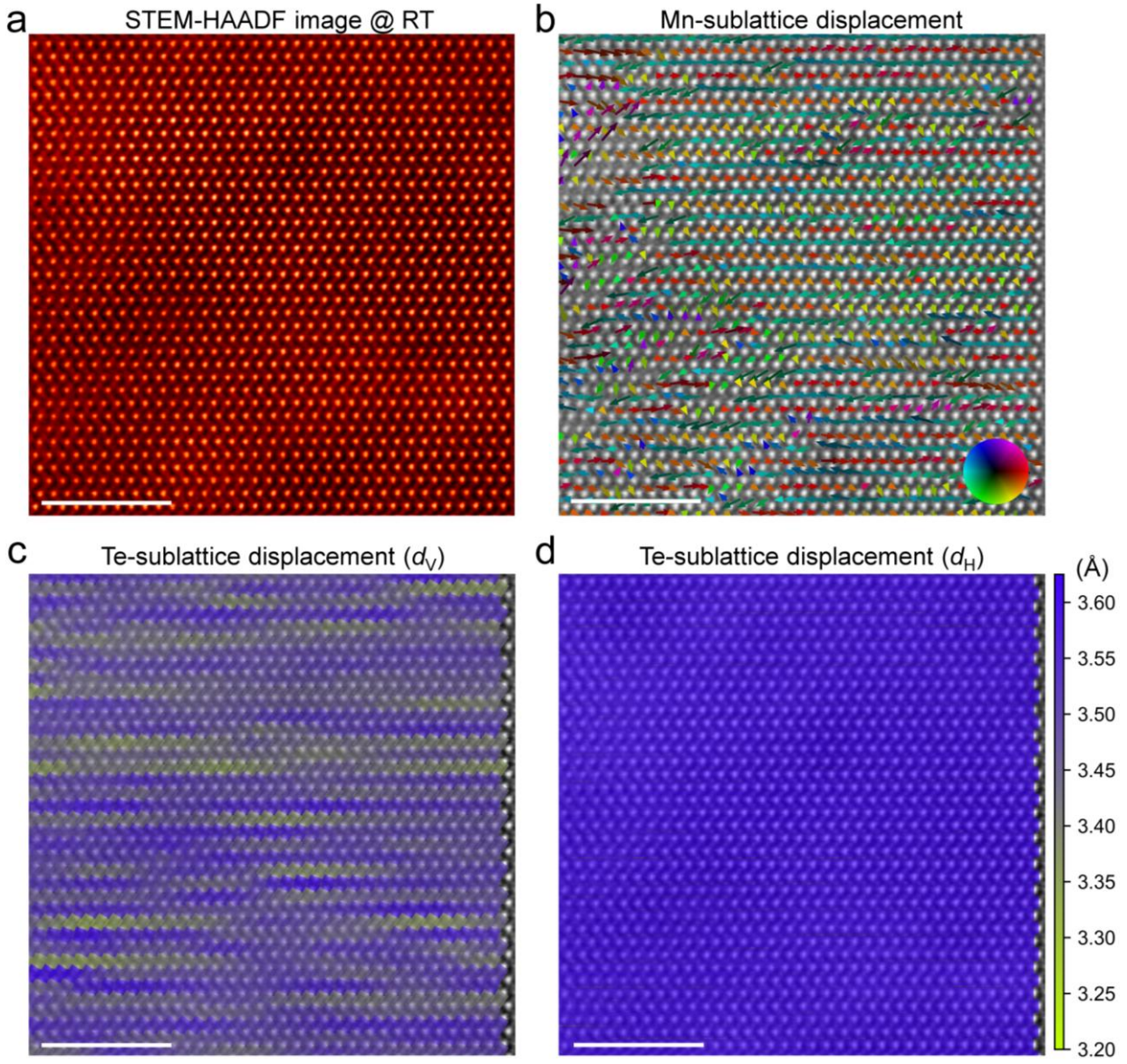


**Figure. S26 α-MnTe lattice structure at room temperature. (a).** A representative STEM-HAADF image showing the atomic structure of α-MnTe along the *a*-axis at room temperature. **(b).** Displacement vector map of the Mn sublattice. The direction and magnitude of Mn displacements

are represented by arrows. **(c).** Modulated Te-Te spacing along the vertical direction ($d_V$) corresponding to the $\Gamma_3^+$ mode. **(d).** Uniform Te-Te spacing along the horizontal direction ($d_H$).

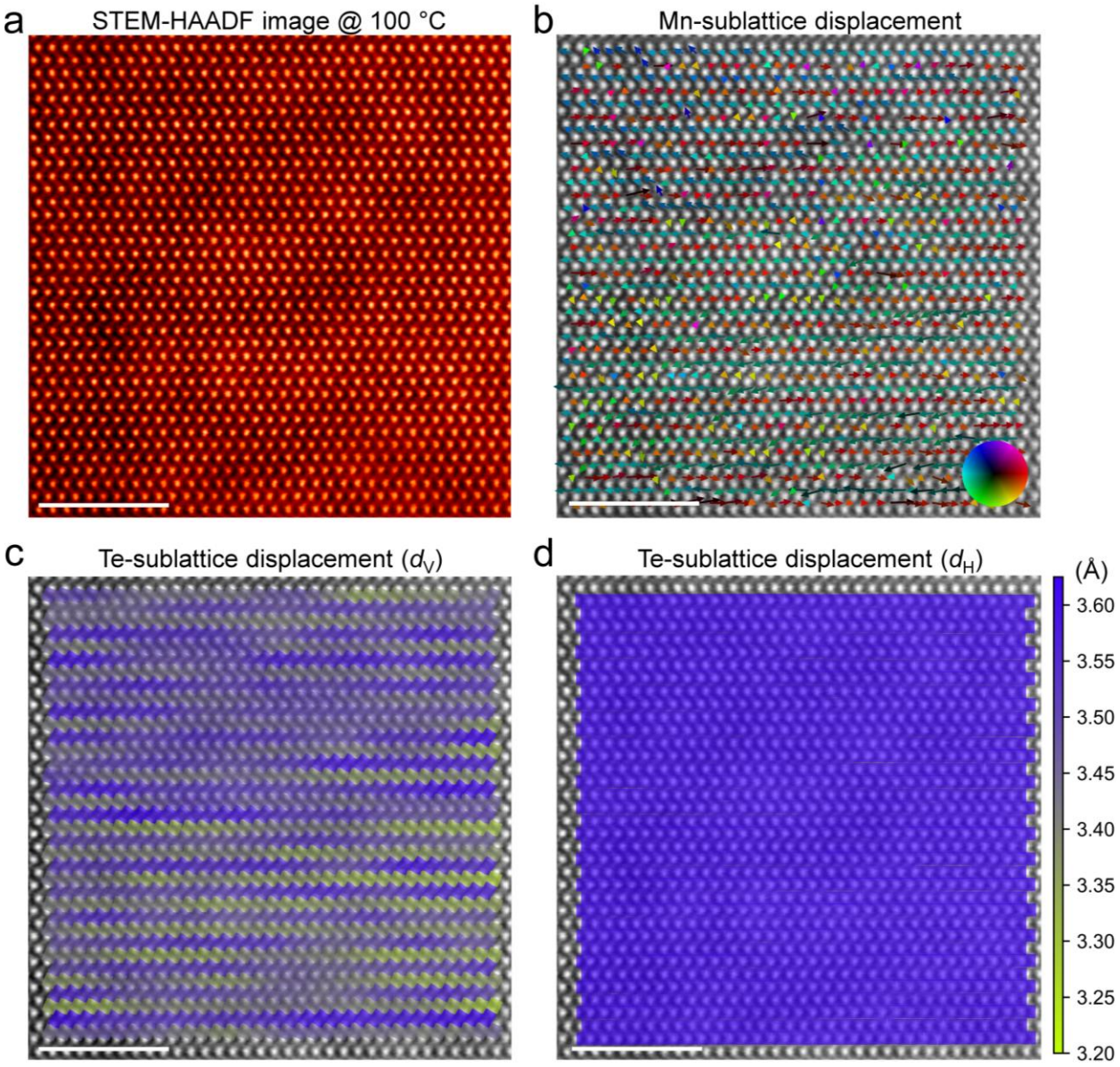


**Figure. S27 α-MnTe lattice structure above the Néel temperature. (a).** A representative STEM-HAADF image showing the atomic structure of α-MnTe along the *a*-axis at 100 °C. **(b).** Displacement vector map of the Mn sublattice. The direction and magnitude of Mn displacements are represented by arrows. **(c).** Modulated Te-Te spacing along the vertical direction ($d_V$) corresponding to the $\Gamma_3^+$ mode. **(d).** Uniform Te-Te spacing along the horizontal direction ($d_H$).

**Reference**


1 Krempaský, J. *et al.* Altermagnetic lifting of Kramers spin degeneracy. *Nature* **626**, 517-522 (2024).

2 Soergel, E. Piezoresponse force microscopy (PFM). *Journal of Physics D: Applied Physics* **44**, 464003 (2011).

3 Collins, L., Liu, Y., Ovchinnikova, O. S. & Proksch, R. Quantitative electromechanical atomic force microscopy. *ACS nano* **13**, 8055-8066 (2019).

4 Labuda, A. & Proksch, R. Quantitative measurements of electromechanical response with a combined optical beam and interferometric atomic force microscope. *Applied Physics Letters* **106** (2015).

5 Song, D. *et al.* Magnetic circular dichroism imaging of atomic-scale antiferromagnetic order at a buried interface. *Nature Nanotechnology* (2026).